POLITECNICO
MILANO 1863

SCUOLA DI INGEGNERIA INDUSTRIALE
E DELL'INFORMAZIONE

A sensitivity analysis of laser-propelled sail trajectories for a mission to Proxima Centauri

TESI DI LAUREA MAGISTRALE IN
SPACE ENGINEERING - INGEGNERIA SPAZIALE

Author: **Federico Infantino**

Student ID: 996989
Advisor: Prof. Camilla Colombo
Co-advisors:
Academic Year: 2022-23

When referring to this work, full bibliographic details must be given, i.e. Federico Infantino, “A sensitivity analysis of laser-propelled sail trajectories for a mission to Proxima Centauri”. 2023, Politecnico di Milano, Faculty of Industrial Engineering, Department of Aerospace Science and Technologies, Master in Space Engineering, Supervisor: Camilla Colombo.

Printed in Italy

Abstract

This work focuses on futuristic gram-scale spacecraft capable of achieving relativistic speeds using laser propulsion systems. It features a numerical propagation of a laser-propelled sail trajectory aiming towards Proxima Centauri, performed to understand trajectory deviations due to initial errors during the propulsion phase. A Relativistic three-body problem, inclusive of the laser acceleration, is implemented to numerically propagate the motion within the Solar System, while the trajectory outside the Solar System is dominated by the Galactic potential model. This model accounts for the gravitational influences of the Galactic bulge, disk, and halo. The mission is indeed segmented into two main phases: the Solar System escape, where the Sun and Earth are the dominant bodies, and the Galactic phase, where the Galaxy becomes the primary gravitational influence. This approach is based on the patched conics method, commonly used in the design of interplanetary missions. The overall model is tested across different mission scenarios, and an optimization is conducted to find the optimal direction of acceleration that minimizes the miss distance with respect to Proxima Centauri at the arrival. The accuracy required in the pointing phase to reach the target star is assessed using Gaussian distributions for initial errors. Furthermore, the magnitude of trajectory deviations relative to input errors is examined, and the success rate of the mission is evaluated based on various initial conditions, aiming to identify the optimal error threshold for maximum launch success.

Keywords: trajectory, interstellar, laser sail, relativistic three-body problem,optimization

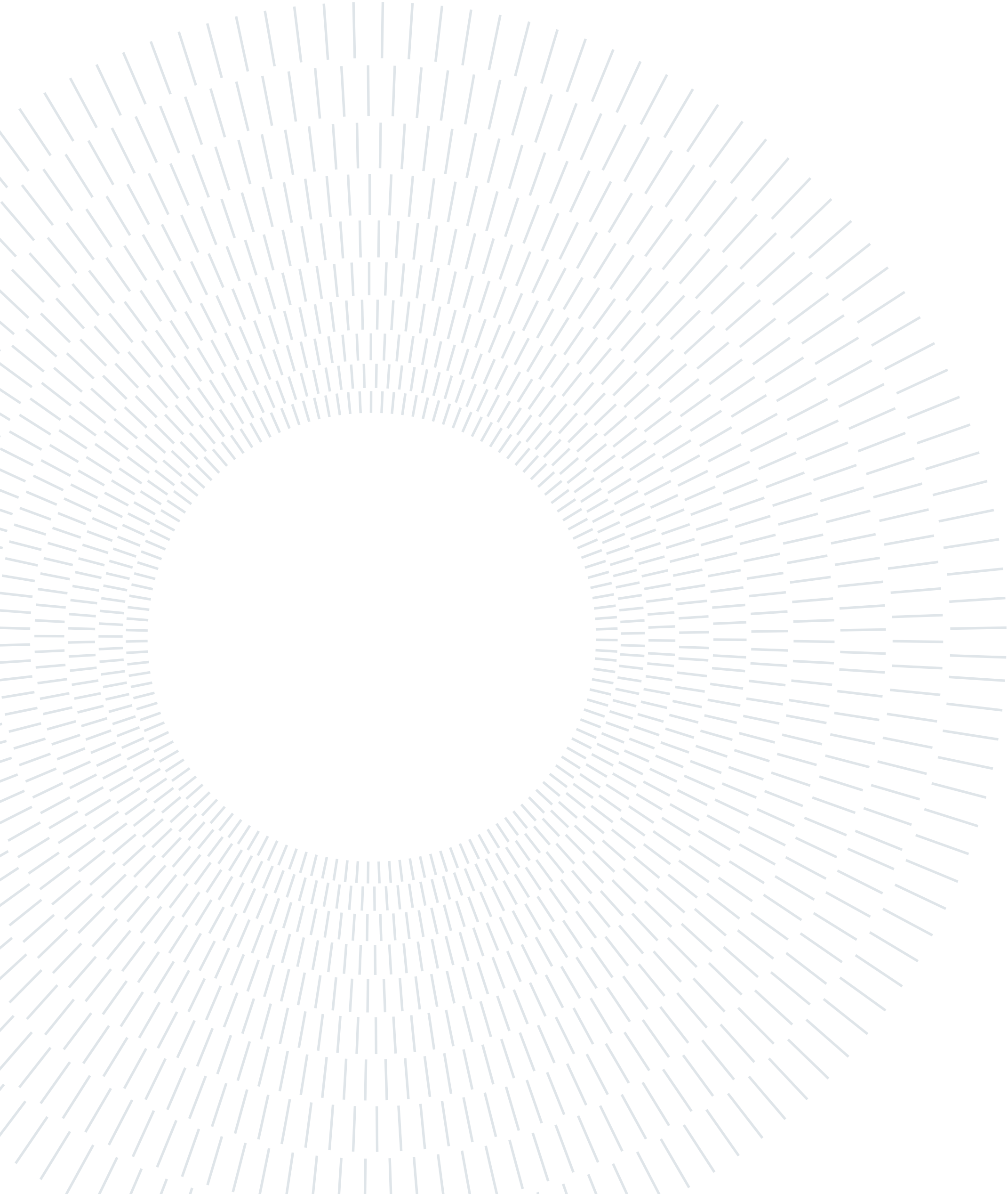

Abstract in lingua italiana

Questo lavoro è basato su vele futuristiche di masse nell'ordine dei grammi, capaci di raggiungere velocità relativistiche utilizzando sistemi di propulsione laser. Si concentra su una propagazione numerica della traiettoria di una vela propulsa da laser in direzione del sistema di Proxima Centauri, al fine di comprendere le deviazioni della traiettoria a causa di errori di puntamento iniziali durante la fase di propulsione. Un problema a tre corpi relativistico, includendo l'accelerazione laser, è implementato per propagare numericamente il moto all'interno del Sistema Solare, mentre la traiettoria al di fuori del Sistema Solare è dominata dalla gravità galattica descritta da un modello di potenziale Galattico. Questo modello tiene conto delle influenze gravitazionali del bulbo, del disco e dell'alone galattico. La missione è suddivisa in due fasi principali: la fuga dal Sistema Solare, dove il Sole e la Terra sono i corpi dominanti, e la fase Galattica, dove la Galassia diventa la principale fonte di influenza gravitazionale. Questo approccio si ispira al metodo delle patched conics, comunemente usato nel design di missioni interplanetarie. Il modello complessivo è testato in diversi scenari di missione, e viene condotta un'ottimizzazione per trovare la direzione ottimale di accelerazione che minimizza la distanza all'arrivo rispetto a Proxima Centauri. L'accuratezza richiesta nella fase di puntamento per raggiungere la stella target è valutata utilizzando distribuzioni Gaussiane per gli errori iniziali. Inoltre, in base alla natura delle deviazioni di traiettoria dovute ad errori iniziali, si valuta il tasso di successo della missione in base a varie condizioni iniziali, al fine di identificare la soglia di errore ottimale al lancio per il massimo successo della missione.

Parole chiave: traiettoria, interstellare, vela laser, problema dei tre corpi relativistico, ottimizzazione

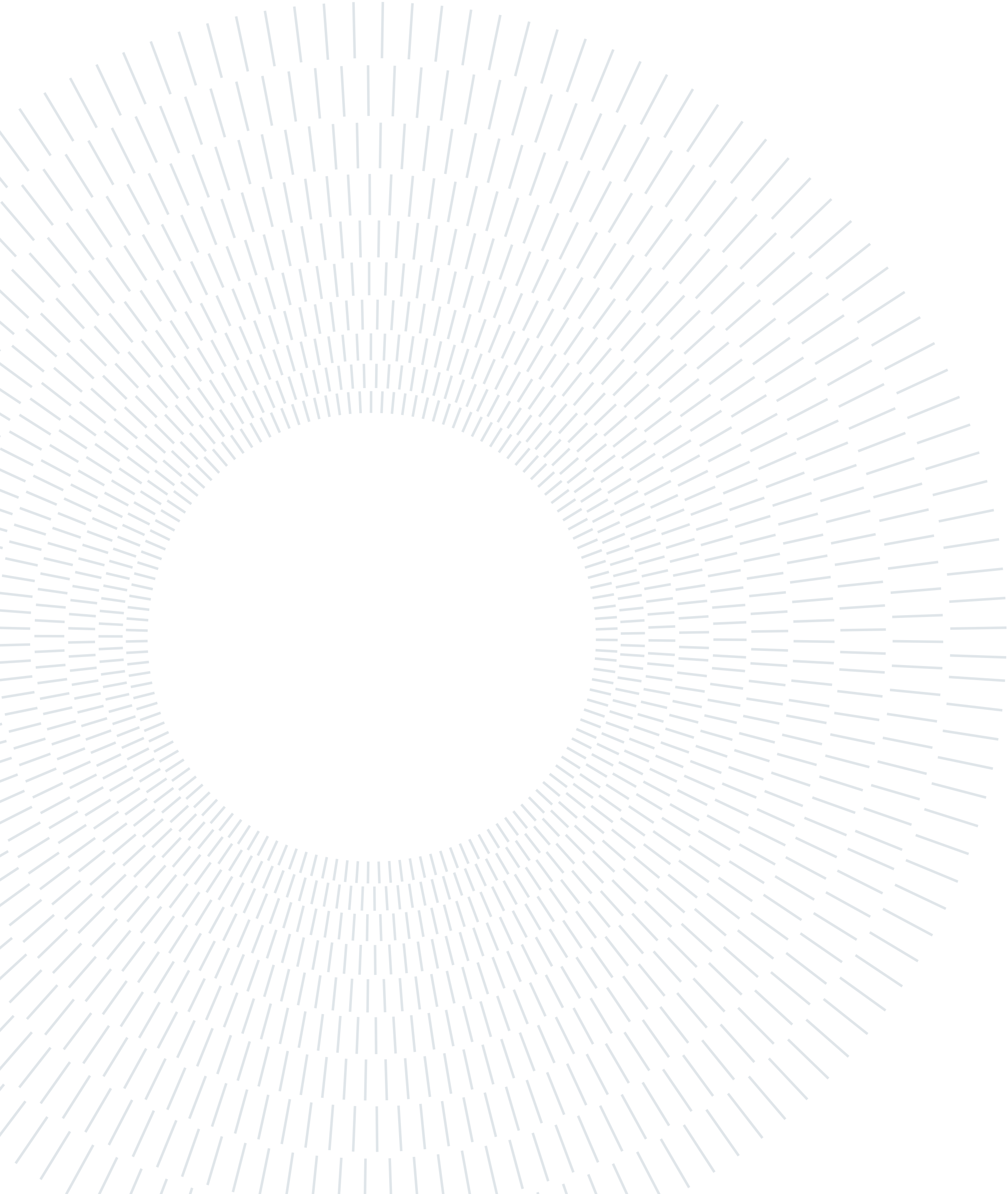

Contents

Introduction

Within decades after the Wright brothers' pioneering flight, humans landed on the Moon, achievement in space exploration previously deemed impossible. Exploration of rocky and gaseous planets, as well as asteroids and moons, followed, pushing us to the boundaries of the Solar System. Our overwhelming nature of exploring the Universe has led to the development of more powerful, safe and controllable rockets able to carry vast arrays of scientific instruments, space station modules and spacecrafts, building the blocks for potential Moon or Mars permanent stations. Chemical propulsion is the key to provide massive thrust levels needed to push human's machines into space. However, despite unimaginable progresses in technology, the idea of an interstellar mission has remained elusive. The vastness of the Universe and the distances among celestial bodies puts in front of us the limitations of our current propulsion systems. Even our fastest spacecrafts, capable of achieving speeds in the order of tenth of km/s, would require thousands of years to reach the nearest star Proxima Centauri. The intrinsic nature of the chemistry and physics of current rocket engines limits the speeds we can achieve; for instance, propelling a 1-gram spacecraft using 10^9 kg of propellant with typical exhaust velocity of ~ 4 km/s, according to the well known Tsiolkovsky's equation [35] :

$$\Delta v = 4\,\mathrm{km/s} \cdot \ln\left(\frac{m_0}{m_f}\right) \approx 0.037\%\, c \tag{1}$$

Where c is the speed of light, m_0 is the initial spacecraft mass (propellant and payload) and m_f the final mass of the spacecraft (without propellant). This simple calculation reveals the inability of even very light spacecraft of reaching relativistic speeds necessary for interstellar travels; thus, the idea of such missions has never been considered feasible. Sometimes, the solution requires a new perspective of the same problem. In the 19th century, Maxwell [27] understood the concept of radiation pressure, but the idea of using it as a propulsion mechanism finds the root with Tsiolkovsky: in 1903, he described the concept of a sail propelled by solar radiation [35]. During the 20th century, many scientists realised that in order to reach relativistic speeds for interstellar travels, probes need to be thinner and lighter, and light itself the propulsion medium. Marx (1966) [25] was one of the first of conceiving the idea of a ground-based laser system capable of accelerate spacecrafts in space, and subsequently Redding (1967) [31] and Forward (1984) [12]. Although some projects were proposed for interstellar travels such as the Project Orion [11], Project Daedalus [6] or Project Longshot [4], Project Dragonfly represents one of the first design studies on laser-propelled interstellar probes, proposed in 2013 by Initiative for Interstellar Studies, and the most recent Breakthrough Starshot (2016) [14] proposed by the Breakthrough Initiatives. This project is based on a directed energy system called DE-STAR (Directed Energy System for Targeting of Asteroids and exploRation) [5], orbital planetary defense system capable of heating of possible hazardous targets, demonstrated potential for propelling gram-scale spacecrafts up to 26% the speed of light [23], reaching Proxima Centauri in ~ 20 years. With advancements in nanophotonics, electronics, and material science, relativistic speeds are within our technological reach [23]. In the following chapters the sail properties are discussed, including the modeling of the laser acceleration and the entire dynamics of the spacecraft, up to the sensitivity analysis of optimal direction of acceleration. These technologies would not only allow the exploration of our neighborhood and close stellar systems and exoplanets, but it would revolutionise the way we explore the Solar System and its boundaries, opening new horizons in the space exploration.

1 | Spacecraft and laser propulsion properties

In this chapter the main properties of the considered spacecraft are showed with few aspects of laser propulsion, without going in details. The aim is to introduce the characteristics of the probe used for the trajectory propagation with its propulsion model. The design choices, optimal properties, and the scaling of the probe mass are treated in the references for this chapter, Lubin [23] as well as Kulkarni et al. [21]. As mentioned in the introduction, the design of an interstellar probe is completely different from what an ordinary spacecraft looks like. A laser sail is made of two main components, the reflector and the spacecraft itself. The duty of the reflector is to reflect most of the incident light to generate the thrust, while the spacecraft is often defined as "watersat", meaning that the components are constructed on a printed circuit board and they could include, for instance, a RTG (Radioisotope Thermoelectric Generator) as power source, nN photon thrusters for small trajectory corrections, the onboard camera, communication devices and other components [23]. This shows that these spacecrafts don't have onboard propulsion systems and then propellant, reducing significantly the mass and also the cost.

1.1. Laser sail

A laser sail has different design considerations compared to the more familiar solar sails. The thickness of reflectors can be on the order of 1-10 μm and the considered density is $\rho = 1440\,\mathrm{kg/m^3}$ [23]. Even low-power lasers can induce extremely high fluxes on a sail, on the order of hundreds of $\mathrm{MW/m^2}$ [23], requiring very high reflectivity coefficients and almost no absorption to avoid extreme temperatures. By using multi-layer dielectric coatings on the laser sail, researchers have achieved less than $\sim 10^{-5}$ absorption, or approximately 99.999% reflectivity [23]. For this study, the ideal case with a reflectivity of $\epsilon_r = 1$ is further assumed. In this work different cases will be presented, from a 2 grams up to 200 grams spacecraft and of course they will be characterized by different dimensions as well as different maximum achievable velocities. Key properties of the considered sails for this work are shown in Table 1.2. It's important to mention that the sail properties are sourced from Lubin [23] (2016), and optimal systems conditions have not been considered. A detailed system model analysis is provided by Kevin L. G. Parkin [29], where design, optimisation, and trade-offs are discussed for the case of the Breakthrough Starshot mission [14].

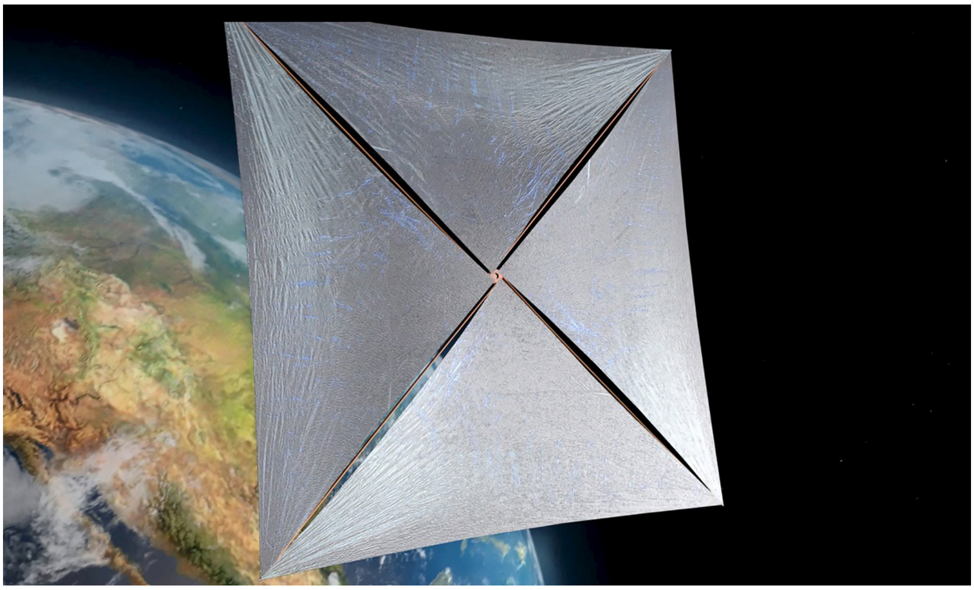

Figure 1.1: A render image of a laser sail. (credits: Breakthrough Starshot, reference: [17])

Thickness (m)	**Side Length (m)**	**Sail Mass (kg)**	**Total Mass (kg)**	**Density (kg/m^3)**
h	**D**	$m_{\mathbf{sail}}$	$m_{\mathbf{sail}} + m_{\mathbf{payload}}$	ρ
10^{-6}	0.85	10^{-3}	$2 * 10^{-3}$	1400
10^{-6}	2.7	10^{-2}	$2 * 10^{-2}$	1400
10^{-6}	8.45	10^{-1}	$2 * 10^{-1}$	1400

Table 1.1: Properties and specifications of the sails.

The side length for a square sail is obtained from Equation 1.1:

$$D = \sqrt{\frac{m_{sail}}{\rho \cdot h}} \tag{1.1a}$$

Where m_{sail} represents the mass of the sail without the payload, while ρ and h the sail material density and thickness, respectively. Table 1.2 shows the considered spacecraft design parameters for this work. Assuming $m_{\text{sail}} = 0.001$ kg and $m_{\text{sail}} = m_{\text{payload}}$, the choice of equal masses for the sail and payload is motivated by optimization considerations, as shown in Appendix A. Such small mass is certainly an optimistic hypothesis, but reasonable with the current state of technology. The design of the sail can be scaled to higher masses up to 10^5kg, and combined with DE-STAR laser systems incredibly high speeds can be achieved, unimaginable for current chemical propulsion systems [23]. Configurations with higher masses can be used, at full scale, for interplanetary applications revolutionizing the way we think a space mission.

1.2. Laser propulsion solutions

In this section the basis of the physics of laser propulsion are introduced. The non-relativistic and relativistic solutions are reported here, with a more complete description in the Appendix A. In the most general case, the magnitude of the force applied by an incident laser on a surface is given by:

$$F = \frac{P(1+\epsilon_r)}{c} \tag{1.2a}$$

where P is the laser power, c is the speed of light and ϵ_r the reflection coefficient, with $\epsilon_r = 0$ for no reflection (all absorbed) and $\epsilon_r = 1$ for complete reflection (for our cases $\epsilon_r \sim 1$) .This equation is valid for a non relativistic approach and when the laser spot is smaller than the sail, meaning that the beam is all incident on surface. Indeed, the laser beam has a footprint of the sail of size:

$$\theta = \text{beam divergence} = \frac{2\lambda}{d} \tag{1.3a}$$

$$D_s = \text{laser spot size} = L\theta = \frac{2L\lambda}{d} \tag{1.3b}$$

where L = distance from laser to sail, θ = beam divergence and d = DE (Directed Energy) array size. This leads to the analysis of two different solutions: when the spot size is smaller than the sail size $D_s < D$ and when is larger $D_s > D$. In addition, when laser propulsion for light sails is considered, speeds in the order of fraction of the light speed can be reached. Thus, the motions of the sails can be affected by relativistic effects, requiring the need of a non-relativistic approach and a relativistic approach for the following solutions.

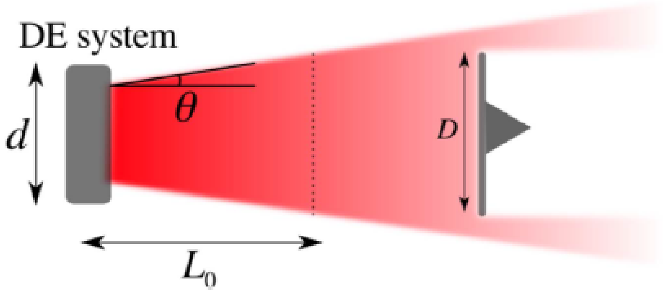

Figure 1.2: A schematic of the Directed Energy system's laser diffraction. At sufficient distances from the system, the beam spills beyond the sail. Here, L_0 is the distance where the laser spot D_s equals the spacecraft size $D.d$ denotes the DE system size, and θ represents the beam divergence. (Kulkarni [21])

$D_s < D$ $non - relativistic\ solution$

This solution is valid for a square sail of side length D with a perfect reflectivity $\epsilon_r = 1$ and DE system size d. Here, $m_{payload}$ is denoted as m_0. From 1.3b the distance L_0 at which $D_s = D$ can be found as:

$$L_0 = \frac{dD}{2\lambda} \tag{1.4a}$$

The kinetic energy needed to reach $L = L_0$ is:

$$E_0 = \frac{1}{2}mv^2 = FL_0 \tag{1.5a}$$

For $\epsilon_r = 1$ we can derive the acceleration from 1.2:

$$a = \frac{F}{m} = \frac{2P}{c(m_{sail} + m_0)} \tag{1.6a}$$

Velocity and acceleration are derived from [23] and showed in detail in the Appendix A :

$$v(L) = \sqrt{\frac{4PL}{c(D^2\, h\, \rho + m_0)}} \tag{1.7}$$

$$a = \frac{2P}{c(D^2\, h\, \rho\, m_0)} \quad \text{(constant while } D_s < D\text{)} \tag{1.8}$$

Defining v_0 as the velocity where $L = L_0$:

$$v_0 = v(L = L_0) = \sqrt{\frac{2PdD}{c\lambda D^2 h\rho}} \tag{1.9a}$$

The time needed to reach this critical condition is:

$$t_0 = \frac{v_0}{a} = \sqrt{\frac{L_0 c D^2 h\rho}{P}} \tag{1.10a}$$

It can be shown in Appendix A that for $m_0 = 0$:

$$v_0 \propto \frac{1}{\sqrt{D}} \tag{1.11a}$$

and accordingly, smaller sails reach higher velocities. While it could be counterintuitive to make small sails and then small reflective surfaces, in this way the mass is reduced. Considering $m_0 \neq 0$, the optimal condition (i.e. the speed is maximized) when $m_0 = m_{sail}$ as shown in Appendix A.

$D_s > D$ non-relativistic solution

If the sail is still illuminated beyond the point L_0 where $D_s = D$, the applied force becomes:

$$F = \frac{2P_0}{c}\left(\frac{L_0}{L}\right)^2 \tag{1.12a}$$

In this domain velocity and acceleration are derived as:

$$v(L) = \sqrt{\frac{2PLdD}{mc\lambda}\left(2 - \frac{L}{L_0}\right)} = v_0\sqrt{2 - \frac{L_0}{L}} \tag{1.13}$$

$$a = \frac{2P}{mc}\left(\frac{L}{L_0}\right)^2 = a_0\left(\frac{L}{L_0}\right)^2 \tag{1.14}$$

From Eq. 1.13, it can be observed that the maximum speed the sail can achieve is given by $v_\infty = v(L = \infty) = \sqrt{2}v_0$. Meanwhile, Eq. 1.14 indicates that the acceleration is no longer constant in this region, and it varies based on the spacecraft's position relative to the DE system.

$D_s < D, D_s > D$ relativistic solutions

The cases mentioned above don't take into account relativistic effects. Approaching relativistic speeds, effects like time dilation, length contraction, wavelength change and effective mass can become severe. Defining the parameter β as the ratio of the spacecraft speed and the speed of light $\beta = v/c$ and the parameter γ (Lorentz factor) as

$$\gamma = \frac{1}{\sqrt{1-\beta^2}} \tag{1.15a}$$

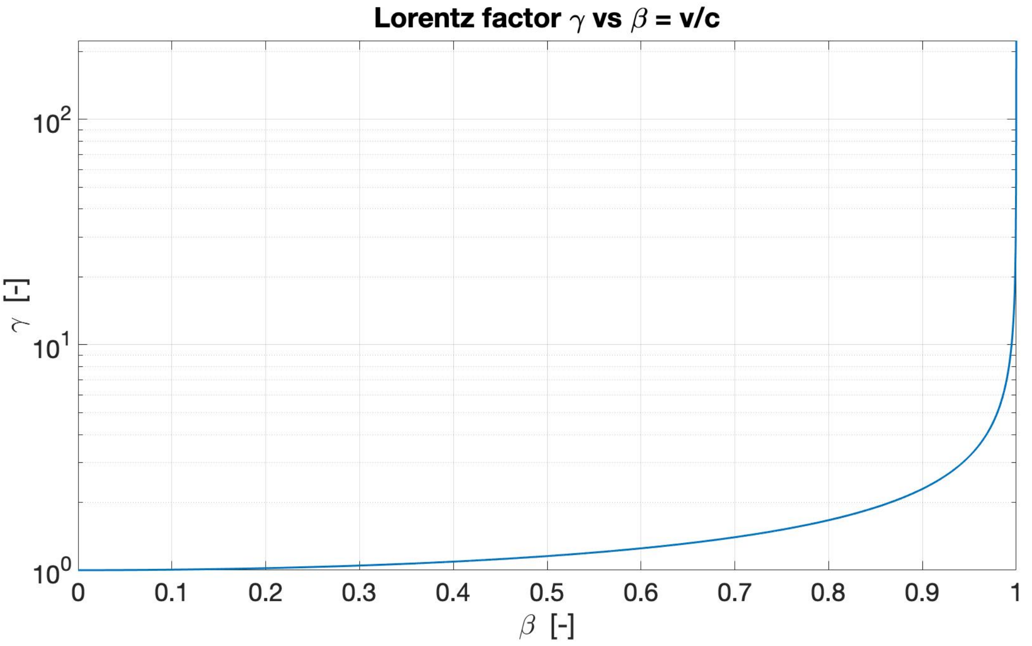

Figure 1.3: Lorentz factor γ vs β factor. γ goes to infinity as $\beta \to 1$

Figure 1.3 shows the values of the Lorentz factor γ for different β values. Even though the relativistic effects become more pronounced as we approach the speed of light, in our cases of $\beta \sim 0.2$ or less, relativistic effects cannot be ignored. This requires a relativistic solution for the spacecraft motion and acceleration. For higher masses, the achievable speeds are smaller than $\beta = 0.2$ and the Lorentz factor is close to the unity. For example, considering the following expression of the effective mass:

$$m_{eff} = m_0 \gamma \tag{1.16a}$$

In this context m_0 is the rest mass. So in the case of $m_0 = 0.002$ kg, a 10 km square DE system with a $P = 100$ GW laser power and with sail optimal conditions ($m_0 = m_{sail}$) a speed of $\beta \sim 0.2$ or $v =\sim 60000 km/s$ can be reached for a propulsion time of $t = 550s$, then $\gamma = 1.0206$ and according to 1.16 the m_{eff} will be 2.0621% higher than the rest mass. Table 1.2 shows the velocities reached for different configurations and the error between the relativistic and non-relativistic solutions.

Sail Mass m [kg]	$\beta_{\textbf{non-rel}}$	$\beta_{\textbf{rel}}$	$\beta_{\textbf{error}}$
10^{-3}	0.236	0.201	17.4%
10^{-2}	0.061	0.058	5.17%
10^{-1}	0.0612	0.0608	0.66%

Table 1.2: Errors on the achievable velocities comparing the relativistic and non-relativistic solutions for sails with properties shown in Table1.2 and a DE system of d = 10 km with a P = 100 GW laser, obtained integrating numerically Eqs. 1.17 for 550s.

Thus, a relativistic solution is shown for the acceleration derived by Kulkarni et al. [21], with a more detailed solution reported in the Appendix A.

$$\begin{cases} \dfrac{2P}{mc^2\gamma^3}\dfrac{(1-\beta)}{(1+\beta)}, & x \leq L_0 \\ \dfrac{2P}{mc^2\gamma^3}\dfrac{(1-\beta)}{(1+\beta)}\left(\dfrac{L_0}{x}\right)^2, & x > L_0 \end{cases} \tag{1.17}$$

P represents the laser system power, β is the ratio of the spacecraft velocity and the speed of light, m is the total mass of the spacecraft, c and γ are the speed of light and the Lorentz factor, while x and L_0 are respectively the distance of the spacecraft from the laser system and the critical distance. In this case the relative distance between the spacecraft and the DE system is denoted as x. The first expression in the region $x \leq L_0$ depends only on the velocity (or β) while the equation for $x > L_0$ depends both on velocity and position x. The use of the relativistic and non-relativistic solutions depend on the achievable velocities of the sails. The relativistic corrections, in a qualitative analysis, can be omitted for $\gamma \sim 1$. Integrating numerically Eqs. 1.17 for different m values in the hypothesis of optimal configuration $m_{sail} = m_{payload}$ the following velocity curves are obtained in Figure 1.4.

Sail thickness (m)	**Spacecraft mass (kg)**	**Sail size (m)**	t_0 **(s)**	L_0 **(m)**	β_0	$\beta_{\mathbf{max}}$
10^{-6}	10^{-3}	0.85	163	4.0×10^9	0.15	0.207
10^{-6}	10^{-2}	2.7	900	1.3×10^{10}	0.091	0.125
10^{-6}	10^{-1}	8.45	4.97×10^3	3.98×10^{10}	0.052	0.073

Table 1.3: Acceleration properties for different sail configurations. L_0 and t_0 represent respectively the distance from Earth's surface and the time to reach the condition where the laser spot size is equal to the sail size and β_0 is the β value at such condition.

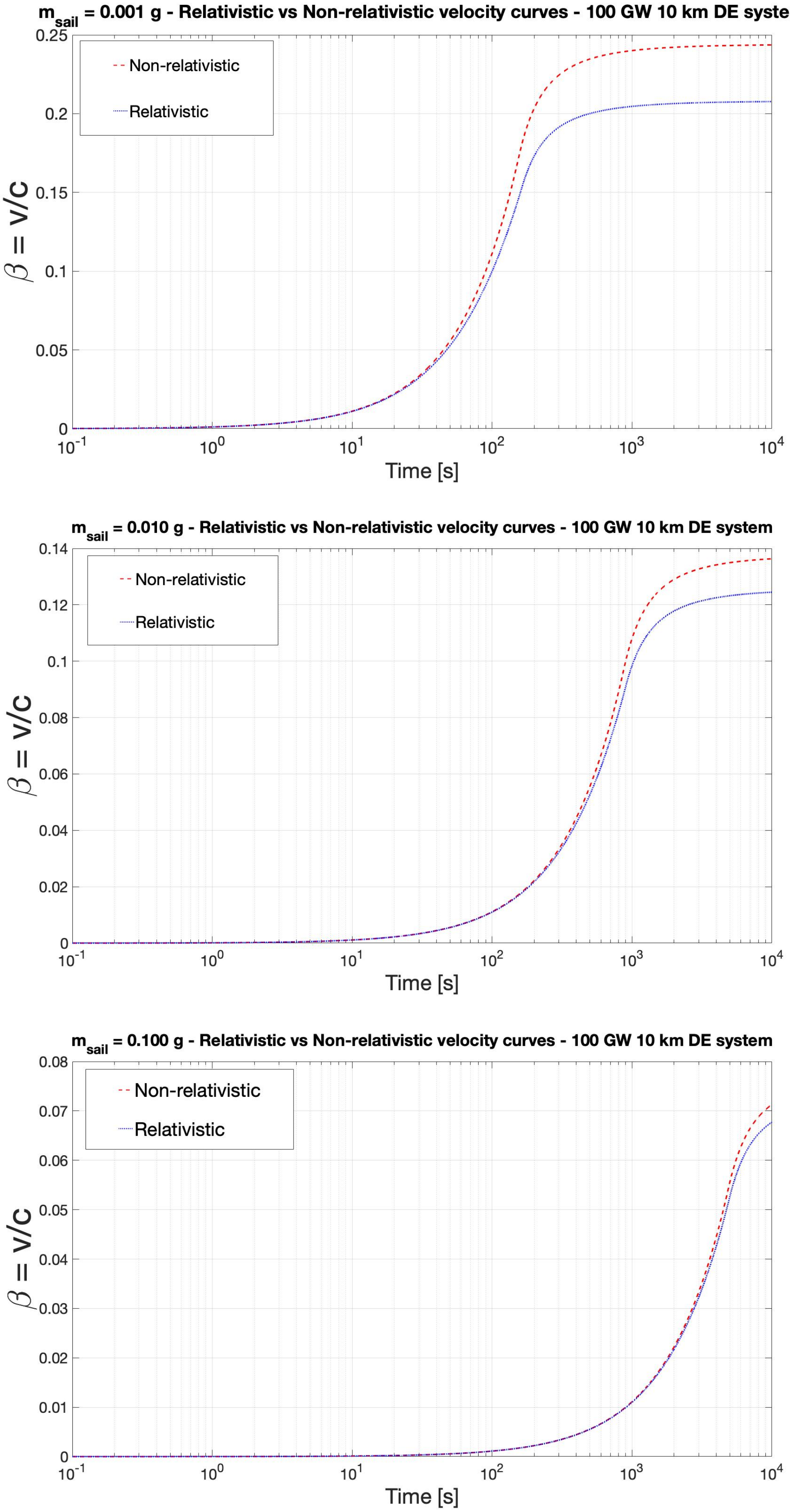

Figure 1.4: Relativistic vs non-relativistic velocity curves for different sail configurations - 100 GW 10 km DE system. For higher masses, the difference becomes less severe for equal propulsion time spans. Optimal conditions are always considered $m_{sail} = m_{payload}$.

1.3. Sail acceleration

In this section the sail acceleration phase is discussed. Even though the Lorentz factor γ becomes smaller as the mass increases, the relativistic solution shown in Eqs. 1.6 will be considered for all cases presented. The spacecraft is in a circular parking orbit at an altitude of $h = 60000$ km from Earth's surface [23] as showed in Chapter 3, and then it's accelerated aiming Proxima Centauri coordinates, in this preliminary analysis. A further step will include the optimization process to determine the optimal direction of acceleration. Here, the velocity curves are shown, while trajectory representations are treated later. The curves are again obtained integrating numerically Eqs. 1.17 with a 10 km DE array size and $P = 100$ GW laser.

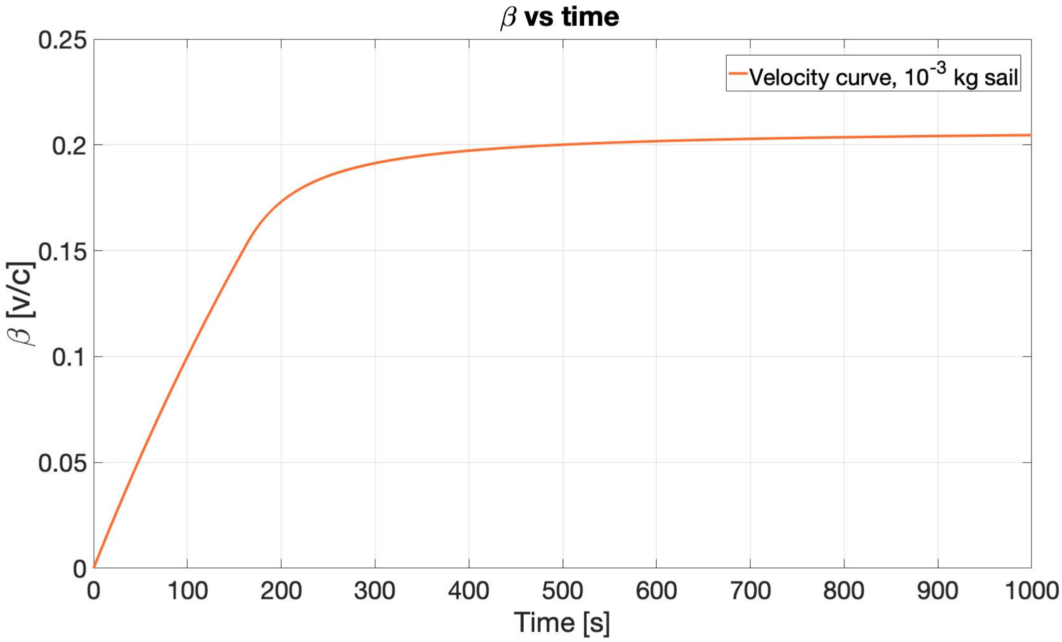

Figure 1.5: Velocity curve in optimal conditions $m_{sail} = m_{payload} = 1g$ with P = 100 GW, d = 10 km. Beyond the distance from laser L_0, the acceleration decreases progressively, and the velocity reaches a maximum value $\sim 0.2c$.

The laser propulsion requires an enormous amount of energy to propel the spacecraft. Here, no optimization is considered for the propulsion time [?]. In this case, the propulsion time is chosen according to the criteria for which the laser is turned off when β variations are no longer significant. For the $m_{sail} = 1g$ case, the propulsion time is chosen to be $t_{propulsion} = 550s$, and for the other cases:

	$m_{\text{sail}} = 10^{-3}$ **kg**	$m_{\text{sail}} = 10^{-2}$ **kg**	$m_{\text{sail}} = 10^{-1}$ **kg**
$t_{\text{propulsion}}$	$550\,s$	$1550\,s$	$4700\,s$
Achieved speed	$20\%\,c$	$11.4\%\,c$	$5\%\,c$
Travel time to Proxima Centauri	$\sim$ 21.2 years	$\sim$ 37.2 years	$\sim$ 84.8 years

Table 1.4: Propulsion times according to the different configurations. It's important to note that higher velocities can be achieved for these cases, but requiring huge propulsion times. In principle, a continued illumination of the sail for the case $m_{sail} = 10^{-1} kg$ would bring the spacecraft up to 7.3% of the speed of light, but the time is chosen to be $4700s$ since beyond this time span the velocity increase is really small.

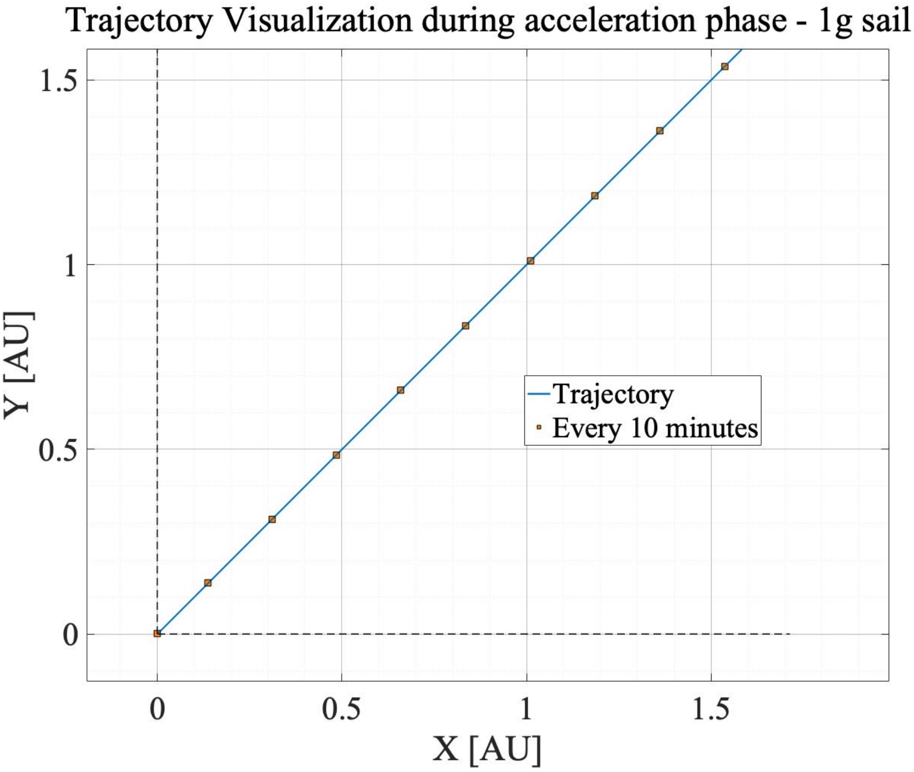

Figure 1.6: Spacecraft trajectory during acceleration phase for $m_{\text{spacecraft}} = m_{\text{sail}} + m_{\text{payload}} = 2g$, P = 100 GW DE system with d = 10km size. The acceleration is pointed to a generic direction in the X-Y plane

As showed in Figure 1.6, during the acceleration phase the trajectory is essentially rectilinear, even though is under the effect of Earth's gravitational influence (within Earth's SOI) and Sun's influence (outside Earth's SOI), the same results are obtained in Lubin 2016 [23]. This would not be true for higher payloads, because the achievable velocities would be smaller. The next figure gives an idea of the speed achieved by the spacecraft and the distance travelled for a time span of $t_{propulsion} = 550s$ for the $m_{sail} = 1g$ case:

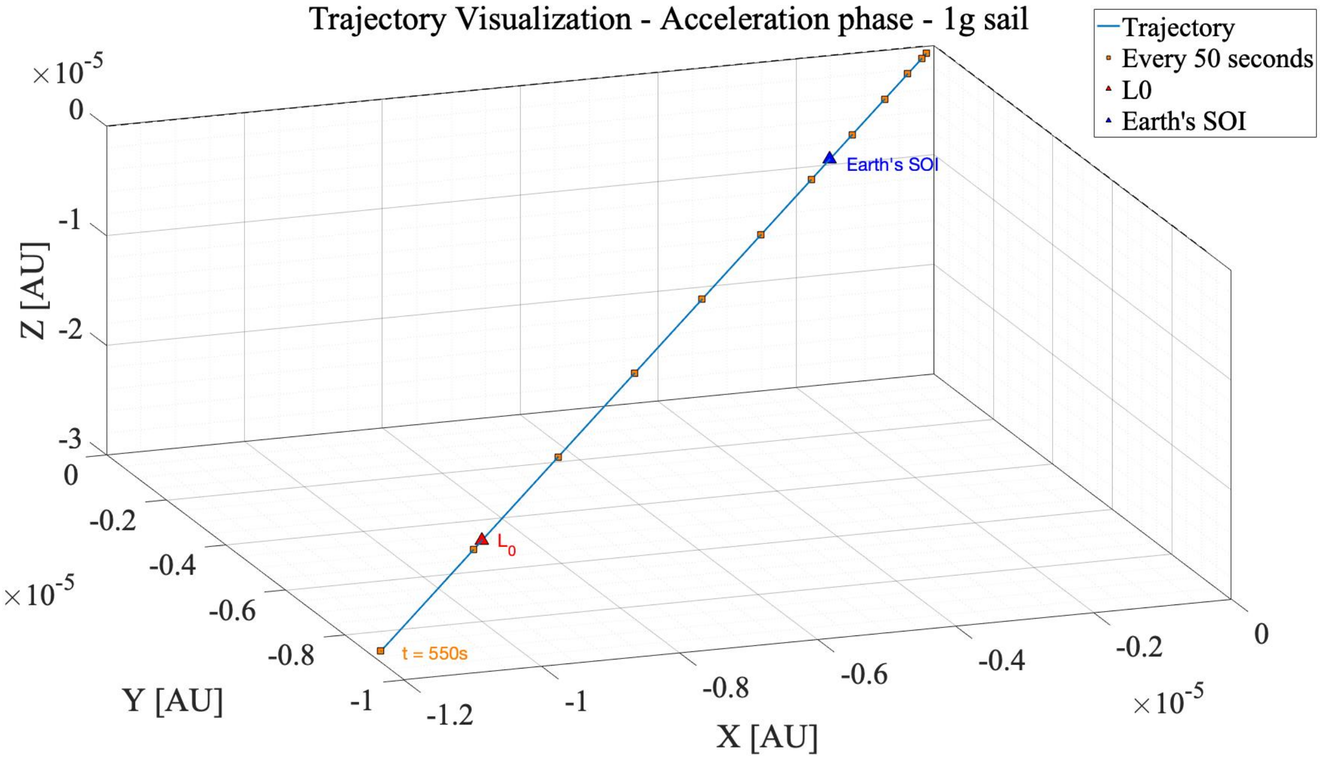

Figure 1.7: Spacecraft trajectory during acceleration phase aiming Proxima Centauri for $m_{\text{spacecraft}} = m_{\text{sail}} + m_{\text{payload}} = 2$ g, P = 100 GW DE system with d = 10 km size. It can be noticed that L_0 is beyond the Earth's sphere of influence. The acceleration phase is also described in Chapter 3.

2 | Alpha Centauri System and the target

The Alpha Centauri system comprises three stars: the solar-like α Centauri A (spectral type G2V, HD 128620), the cooler dwarf α Centauri B, and Proxima Centauri (HIP 70890, GJ551) [20]. Proxima Centauri stands out as the closest star to our Sun, situated at a distance of d = 4.24 light years [13]. The solar neighborhood encompasses over 150 stars within a 20 light-year radius from the Sun, and some of these stars harbor potentially habitable exoplanets [23].

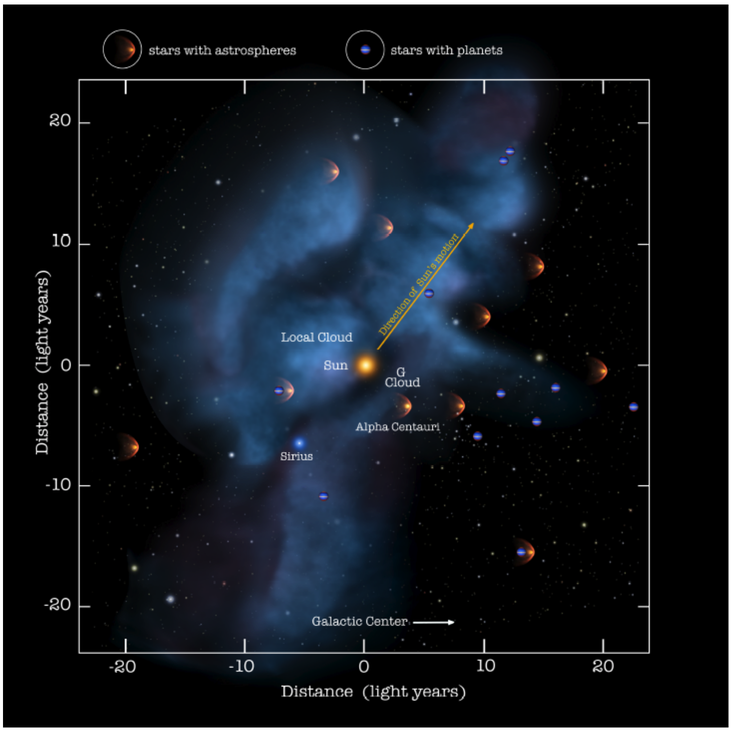

Figure 2.1: Stars and structures within approximately 25 light years of Earth. As indicated, some nearby stars are already known to contain planets and planetary systems that are potential targets. NASA/Goddard/Adler/U. Chicago/Wesleyan [32].

The target considered in this work, as well as for the Breakthrough Starshot mission

[14], is the red dwarf Proxima Centauri. The reason for this choice, besides its proximity to Earth, is linked to the discovery of a potentially habitable planet named Proxima b [2]. Recent studies on the habitability of Proxima b though, have been questioned the development of life in the exoplanet due to the star's activity [33]. Nevertheless, there are a lot of uncertainties on the possibility of life on the planet and Proxima Centauri with its exoplanet Proxima b are one of the main targets for interstellar missions.

2.1. Proxima Centauri's coordinates in the equatorial frame

The coordinates of an object in the Universe, like a star, are typically expressed in the equatorial frame: the right ascension α, declination δ, the parallax π, the proper motions $\mu_{\alpha*}$ and μ_δ and the radial velocity v_r. Although only α and δ can be used to define the direction (unitary vector) of the star in the equatorial frame, the other parameters are fundamental to represent the star's motion. For this work, the full 6D data of the star are taken from ESA GAIA mission (Data Release 3) [13] and can be summarized in the following table:

Proxima Centauri's coordinates

Parameter	**Value**	**Unit**
Right ascension α	217.392 ± 0.024	degrees
Declination δ	-62.676 ± 0.034	degrees
Parallax π	768.067 ± 0.050	mas
Proper motion RA $\mu_{*\alpha}$	-3781.741 ± 0.031	mas/year
Proper motion Dec μ_δ	769.465 ± 0.051	mas/year
Radial velocity v_r	-21.943 ± 0.216	km/s

Table 2.1: **Note**: The provided parameters are given in the International Celestial Reference System (ICRS) with the reference epoch of J2016.0. The Gaia-CRF3 is defined by the positions and proper motions at epoch 2016.0 for a specific set of extragalactic sources in the DR3 catalogue. It comprises about 1.6 million QSO-like sources and provides a high-precision astrometric framework. Further details and technical insights can be found in the referenced article [8].

From Table 2.1, we can get the direction of Proxima Centauri with respect to Earth in

ICRS reference system, as well as its heliocentric distance:

$$x_{P_{ICRS}} = \cos(\delta)\cos(\alpha) \tag{2.1a}$$

$$y_{P_{ICRS}} = \cos(\delta)\sin(\alpha) \tag{2.1b}$$

$$z_{P_{ICRS}} = \sin(\delta) \tag{2.1c}$$

$$d_P = \frac{1}{\pi} = 1.3020\,pc \tag{2.1d}$$

Where the subscript P denotes Proxima C. The evaluation of the heliocentric distance by inversion of the parallax is in general not compatible with GAIA measurements due to the errors associated with the measurements and its consequent non-linearity [24]. Indeed, this would lead to a biased distance estimate since the transformation between parallax and distance is non-linear, requiring other techniques to evaluate the heliocentric distance [24]. However, Proxima Centauri has a very precise parallax measurement: 768.0665391873573 ± 0.049872905 mas, so that the signal to noise ratio exceeds 15000 [13] and the the non-linear aspect in the parallax-distance conversion can be ignored [24]. As mentioned before, the parameters in Table 2.1 are expressed using ICRS frame. The ICRS differs from the Equatorial frame because it's an inertial frame based on positions of extra-galactic sources considered almost fixed, so it's more stable than the equatorial frame [8]. For this application, where a qualitative direction and position of Proxima Centauri's is required, the distinction between ICRS and equatorial frame can be ignored. The Proxima Centauri's equatorial heliocentric position is then defined as:

$$\mathbf{r}_{P,h} = d_P \begin{bmatrix} x_P \\ y_P \\ z_P \end{bmatrix} = \begin{bmatrix} -0.4748 \\ -0.3629 \\ -1.1567 \end{bmatrix} \text{ pc} \tag{2.2}$$

where pc represents parsecs. This vector has to be rotated and moved into a galactocentric coordinate systems to evaluate the galactic gravitational forces. A detailed description of the orientation of galactic frame is given by Liu, Zhu & Zhang [22] (2011). Following the procedure showed in [10], the rotation matrices involved are:

$$\mathbf{R_x} = \begin{bmatrix} 1 & 0 & 0 \\ 0 & \cos(\theta_x) & \sin(\theta_x) \\ 0 & -\sin(\theta_x) & \cos(\theta_x) \end{bmatrix} \tag{2.3}$$

$$\mathbf{R_{z1}} = \begin{bmatrix} \cos(\theta_{z1}) & \sin(\theta_{z1}) & 0 \\ -\sin(\theta_{z1}) & \cos(\theta_{z1}) & 0 \\ 0 & 0 & 1 \end{bmatrix} \tag{2.4}$$

$$\mathbf{R_{z2}} = \begin{bmatrix} \cos(\theta_{z2}) & \sin(\theta_{z2}) & 0 \\ -\sin(\theta_{z2}) & \cos(\theta_{z2}) & 0 \\ 0 & 0 & 1 \end{bmatrix} \tag{2.5}$$

Where $\theta_{z2} = 90 + \alpha_0$, $\theta_x = 90 - \delta_0$ and $\theta_{z1} = 90 - \theta$. $\theta = 122.93$ deg, $\alpha_0 = 192.86$ deg and $\delta_0 = 27.13$ deg are the positional angle and North Galactic Pole equatorial coordinates defining the Galactic frame orientation while $\mathbf{R_x}$ and $\mathbf{R_{z1,z2}}$ denote the rotation with respect to OX and OZ axes, respectively [10]. The heliocentric position vector of Proxima Centauri, but in galactic coordinates, is obtained in Eq. 2.7 rotating the heliocentric equatorial vector and aligning it to the galactic frame:

$$\mathbf{A_G} = \mathbf{R_{z1}}\mathbf{R_x}\mathbf{R_{z2}} \tag{2.6}$$

$$\mathbf{R_{P,h,galactic}} = \mathbf{A_G}\,\mathbf{r_{P,h}} = \begin{bmatrix} 0.2687 \\ 1.2601 \\ -0.1873 \end{bmatrix} \text{ pc} \tag{2.7}$$

vector eventually moved from the Sun to the Galactic Centre, by adding the position of the Sun:

$$\mathbf{R_P} = \mathbf{R_{P,h,galactic}} + \mathbf{R_{sun}} = \begin{bmatrix} -8399.7 \\ 1.2601 \\ 16.8127 \end{bmatrix} \text{ pc} \tag{2.8}$$

where $\mathbf{R_{sun}} = (-8400, 0, 17)$ pc [10] is the position vector of the Sun in Galactocentric coordinates.

2.1.1. Star's measurement errors

Even though the coordinates from ESA Gaia mission are really precise, measurements are subjected to errors and the the real Proxima Centauri's position is uncertain. Indeed, rather than a point in space, a volume error in the physical space should be introduced to describe the region within which Proxima Centauri probably lies. The estimation of the volume error in a real 3D space is not trivial, since the astrometric parameters have been derived in a single fitting process such that the errors are correlated, and the full covariance matrix should be used to include the errors in the measurements process as shown in the following ESA document [7]. In the case presented in this work, the nominal values are considered to compute the target direction for the mission, according to the star's motion as described in section 2.2.

2.2. Proxima Centauri's motion

As every celestial body in the Galaxy, Proxima Centauri is orbiting around the Galaxy and moving with respect to the Solar System. This is crucial when the spacecraft is accelerated, since it has to be pointed to the future location of Proxima Centauri with respect to the departure date. The coordinates and motion parameters shown in Table 2.1 are referred to a ICRS with the reference epoch of J2016.0. Assuming that the launch of the sail takes place on that date, according to Proxima Centauri's motion with respect to Earth its position vector will change during the travel. The Gaia ESA Archive, contains the function "Epoch Prop", which is specifically designed to propagate the positions of stars from a reference epoch to a specified future epoch, accounting for the full covariance matrix [9]. This capability is crucial for accurate long-term studies and predictions of stellar motions, as the case considered for this work where in missions with duration of several years the star's motion is relevant. According to such propagation function, the target positions in a heliocentric equatorial frame including the star's motion are:

Case 1: $m_{sail} = 1g$ Travel time : $21.2\,years$

$$\mathbf{r}_{P,h,1} = d_P \begin{bmatrix} x_P \\ y_P \\ z_P \end{bmatrix} = \begin{bmatrix} -0.4750 \\ -0.3624 \\ -1.1562 \end{bmatrix} \text{ pc} \tag{2.9}$$

Comparing this result with Eq. 2.2, we can observe that Proxima Centauri moves approximately 144 astronomical units (AU) relative to the Sun within a span of 21.2 years. It's crucial to bear in mind that this doesn't represent the exact future position of Proxima Centauri but rather the target position we consider for this case. As mentioned in subsection 2.1.1, measurement errors prevent us from localizing an exact point in space for a star; instead, it results in a volume centered around the nominal position shown in Eq. 2.11.

Case 2: $m_{sail} = 10g$ Travel time : $37.2\,years$

$$\mathbf{r}_{P,h,2} = d_P \begin{bmatrix} x_P \\ y_P \\ z_P \end{bmatrix} = \begin{bmatrix} -0.4752 \\ -0.3621 \\ -1.1559 \end{bmatrix} \text{ pc} \tag{2.10}$$

Case 3: $m_{sail} = 100g$ Travel time : $84.8\,years$

$$\mathbf{r}_{P,h,3} = d_P \begin{bmatrix} x_P \\ y_P \\ z_P \end{bmatrix} = \begin{bmatrix} -0.4756 \\ -0.3610 \\ -1.1548 \end{bmatrix} \text{ pc} \tag{2.11}$$

To give an idea, in this last case, over a span of 84.8 years the star would move ~ 86.67 billion kilometers or ~ 579 AU relative to the Sun.

3 | Dynamics and trajectory

3.1. Mission overview

In this chapter the equations and the mathematical models used to propagate the trajectory are presented. The considered approach gets inspiration from the patched conics method, similarly to what is done in interplanetary missions design. The idea behind the patched conics method is to break down a mission trajectory into distinct segments, each dominated by the gravitational influence of a singular celestial body. This influence is often represented by the concept of the 'Sphere of Influence' (SOI)— a region around a celestial body where its gravitational forces dominate over others [3]. The considered mission in this work consists of three main phases and a fourth one, the arrival, that is not treated and modelled:

- **Acceleration phase**. This represents the departure segment, where the spacecraft is accelerated with laser aiming the target direction. During this phase, the sail crosses the Earth's SOI and it's affected by Sun's and Earth's gravitational fields.
- **Heliocentric trajectory**. This phase consists of the spacecraft's trajectory within the Solar System and the chasing of its boundary, represented by the Solar System Hill sphere.
- **Galactic trajectory**. In this segment the spacecraft is outside the Solar System sphere of influence and its trajectory is influenced by the galaxy's gravitational field.
- **Arrival**. This would be the last segment of the spacecraft's journey, where the dominant bodies would be Proxima Centauri and Alpha Centauri A and B.

Each of those will be analyzed in detail in different sections. The segmentation of the full trajectory can give a more comprehensive description of the dynamics of the spacecraft when a certain gravitational force is acting on it.

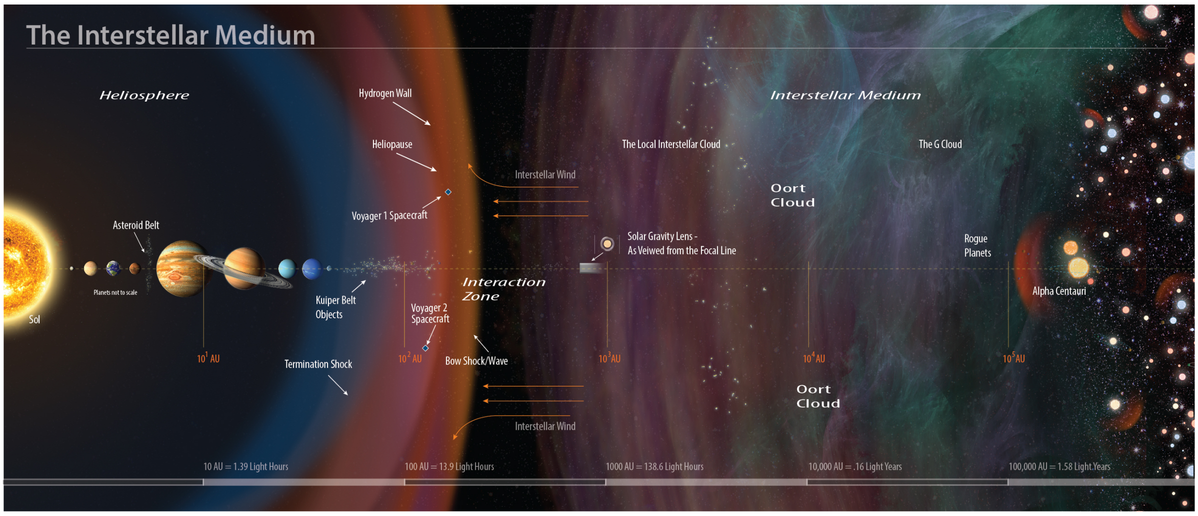

Figure 3.1: An illustration of the complex environment between the Solar System and the Alpha Centauri System. All the matter and radiation between the stars is called Interstellar Medium (ISM). Credit; Charles Carter/Keck Institute for Space Studies

As shown in Chapter 2, Section 1.3, the trajectory is expected to be rectilinear primarily due to the high speeds achieved with DE propulsion systems. Therefore, the challenge is to accelerate the spacecraft in a direction that, taking into account gravitational effects, would bring the spacecraft to the target. Pointing errors during the acceleration phase can result in significant deviations upon arrival, potentially causing the spacecraft to miss the target completely. The considered spacecrafts do not possess onboard propulsion systems capable of correcting such trajectory errors; instead, minor trajectory corrections and attitude adjustments, as described later in this chapter, are employed.

The primary source of deviation from the target in this work is gravity. Other disturbances, such as interplanetary and interstellar dust and particles, or the effects of the intergalactic magnetic field, are assumed to be compensated for by the spacecraft itself through counteracting methods discussed in Lubin [23]. In fact, the objective of this work is not to analyze a highly complex mission scenario, but rather to develop a model to simulate a trajectory and investigate its sensitivity to errors during the boosting phase.

In the following sections, the gravitational models used to propagate the trajectory will be presented and discussed. The acceleration of the sail through the laser system is initially optimized to reach the target while accounting for all gravitational perturbations, in order to identify the optimal direction of acceleration. Subsequently, we will consider initial errors and study how the trajectory would be affected in terms of miss distances from the target.

3.2. Parking orbit and initial spacecraft's state vector

At the beginning of the journey, the spacecraft is assumed to lie in a $h = 60000$ km circular parking orbit as described in Parkin (2018) [29]. The initial state vector is here arbitrarily chosen for simplicity and doesn't reflect a real mission scenario. The mission is assumed to take place on January 1, 2016, to ensure consistency with the direction measurements of Proxima Centauri given by the ESA GAIA archive [13]. The initial position vector is assumed to be aligned in the target direction of the star (see Sec. 2.2) as shown in the following figure:

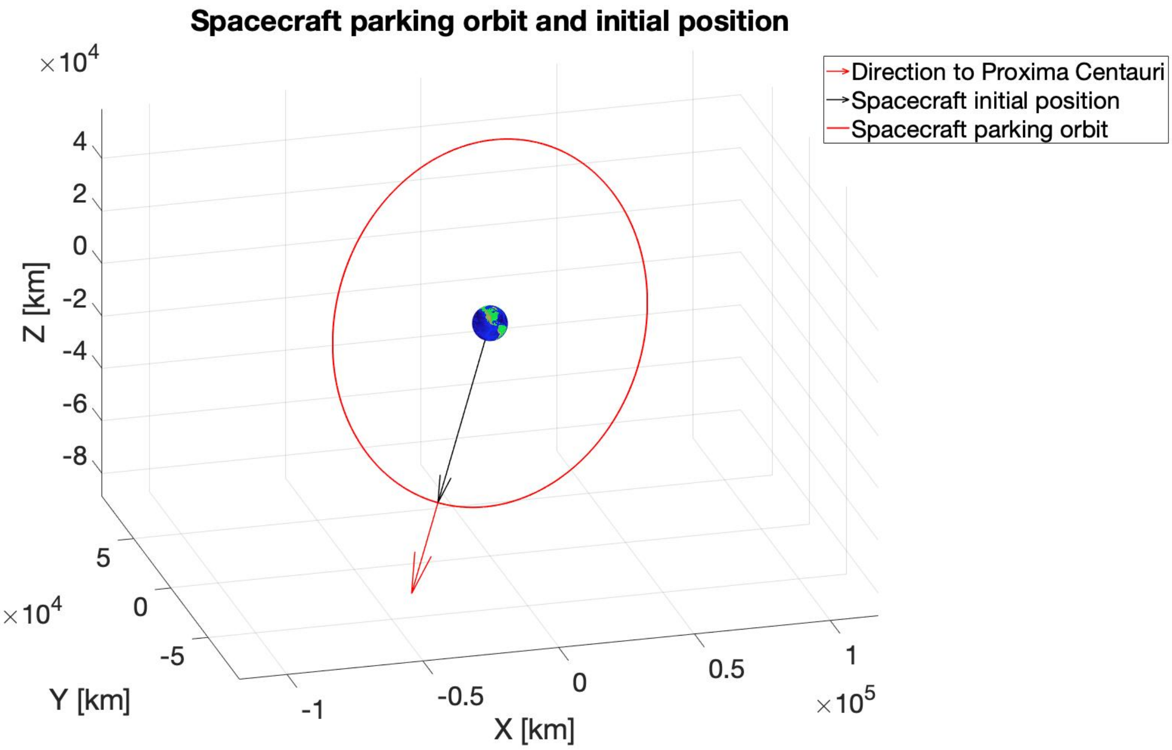

Figure 3.2: Spacecraft parking orbit in an equatorial geocentric frame. The spacecraft is propelled starting from the point on the orbit aligned with the target direction. The case shown here is the first one (21.2 years duration), meaning that the target is defined according to the estimated position of Proxima Centauri 21.2 years from the departure date (J2016.0).

$$\mathbf{s}_0 = \begin{bmatrix} \mathbf{r_0} \\ \mathbf{v_0} \end{bmatrix} \quad \text{where} \quad \hat{\mathbf{r}}_0 = \hat{\mathbf{dir}}_{\mathbf{target}} \tag{3.1}$$

The initial state vector is then chosen according to the target directions described in Section 2.2. These initial conditions represent an initial guess for the direction of acceleration when an optimization process will be performed later in this work, in order to reach the target with the minimum miss distance possible. Indeed, accelerating the spacecraft aiming at the future position of the star is not the correct approach to reach the target because the spacecraft would be deviated from the nominal trajectory by gravity as well as by the motion of the Sun with respect to the Galaxy, as will be discussed later.

3.3. Acceleration phase and heliocentric model

The physics of the acceleration phase is qualitatively described in Section 1.3, including the choice of the propulsion time, the achievable velocity and the velocity curve. The motion of the spacecraft is modeled using the Restricted Three-Body Problem, accounting for the spacecraft's trajectory from a parking orbit around Earth. During acceleration, the spacecraft exits Earth's Sphere of Influence (SOI) and initially encounters the dominant gravitational forces of Earth. As it progresses, the Sun's gravitational influence becomes prevalent. This model simplifies the complex gravitational interactions in space by primarily considering the Earth and the Sun, despite the fact that other celestial bodies, including the Moon and other planets, also affect the spacecraft's trajectory. For a mission that starts around Earth and extends to the boundary of the Solar System, this simplification is reasonable. To align more closely with reality, relativistic effects are also included, particularly since they become significant for a spacecraft with a mass on the order of a few grams where the velocities are up to 20% the speed of light. Contrasting with classical Newtonian mechanics, these effects could greatly influence the motion equations. Moreover, the spacecraft is subject to low-thrust laser acceleration, which is not impulsive but rather gradual and dependent on time, despite the propulsion times being short relative to the mission's duration. Indeed, during the acceleration phase, the spacecraft traverses billions of kilometers, making the gradual change in velocity (Δv) due to laser acceleration a critical aspect of the motion model. The spacecraft's acceleration is modelled as follows:

$$\mathbf{a_{sc}} = \mathbf{a_{gravity}} + \mathbf{a_{laser}} \tag{3.2}$$

where $\mathbf{a_{laser}}$ acts only during the propulsion times discussed in section 1.3 and is pointed with the optimal direction that will be discussed later. The model used to describe the gravitational influence $\mathbf{a_{gravity}}$ including relativistic effects comes from Masat [26], that provides a solution for a relativistic N-Body problem and is reported here:

$$\ddot{\mathbf{r}}_i = \ddot{\mathbf{r}}_{\mathrm{Newt},i} + \mathbf{a}_{\mathrm{Rel},i} + \sum_{j\neq i}\left(c_1\mathbf{M}_{ij}^{①} + c_2\mathbf{M}_{ij}^{②}\right)\ddot{\mathbf{r}}_j \tag{3.3}$$

This model integrates Newtonian gravitational forces with relativistic corrections from General Relativity. The acceleration $\ddot{\mathbf{r}}_i$ for a body i includes Newtonian attraction $\ddot{\mathbf{r}}_{\mathrm{Newt,i}}$ and relativistic terms $\mathbf{a}_{\mathrm{Rel},i}$, the latter being significant at high velocities or near massive bodies. Matrices M_{ij}^1 and M_{ij}^2, weighted by constants c_1 and c_2, encode the system's interdependent motions, reflecting relativistic effects. From Eq. 3.3 it can be derived the specific equation for this application, where i = spacecraft and the bodies j acting on it are the Sun and Earth. Expanding the term $\ddot{\mathbf{r}}_{\mathrm{Newt,i}}$ for a restricted Three Body Problem centred in the Sun, according to the formulation in Vallado [36]:

$$\ddot{\mathbf{r}}_{\mathrm{Newt,sc}} = -\frac{Gm_{\odot}}{r^3}\mathbf{r} - Gm_{\oplus}\left(\frac{\mathbf{r}_{\oplus\mathrm{sc}}}{r_{\oplus\mathrm{sc}}^3} + \frac{\mathbf{r}_{\odot\oplus}}{r_{\odot\oplus}^3}\right) \tag{3.4}$$

Where $\mathbf{r}$ is the position vector of the spacecraft in a heliocentric frame. In Equation (3.4), the acceleration of a spacecraft in a restricted three-body system is described. The first term on the right side represents the gravitational pull on the spacecraft by the Sun, while the second and third terms encapsulate respectively the direct effect of the third body (Earth) on the spacecraft and the indirect effect of Earth on the Sun. The vector $\mathbf{r}_{\oplus\mathrm{sc}}$ represents the position of the spacecraft with respect to Earth, and $\mathbf{r}_{\odot\oplus}$ represents the position of Earth with respect to the Sun. The expression of $\mathbf{a_{Rel,i}}$ looks very complex and the general expression is reported here [26]:

$$\begin{aligned}\mathbf{a}_{\mathrm{Rel},i} = &\sum_{j\neq i}\frac{\mu_j}{r_{ij}^3}(\mathbf{r}_j - \mathbf{r}_i)\Bigg\{-\frac{4}{c^2}\sum_{k\neq i}\frac{\mu_k}{r_{ik}} - \frac{1}{c^2}\sum_{k\neq j}\frac{\mu_k}{r_{jk}} + \left(\frac{v_i}{c}\right)^2 \\ &+2\left(\frac{v_j}{c}\right)^2 - \frac{4}{c^2}(\dot{\mathbf{r}}_i\cdot\dot{\mathbf{r}}_j) - \frac{3}{2c^2}\left[\frac{(\mathbf{r}_i - \mathbf{r}_j)\cdot\dot{\mathbf{r}}_j}{r_{ij}}\right]^2\Bigg\} \\ &+\frac{1}{c^2}\sum_{j\neq i}\frac{\mu_j}{r_{ij}^3}\left\{[\mathbf{r}_i - \mathbf{r}_j]\cdot[4\dot{\mathbf{r}}_i - 3\dot{\mathbf{r}}_j]\right\}(\dot{\mathbf{r}}_i - \dot{\mathbf{r}}_j)\end{aligned} \tag{3.5}$$

In this case of a restricted heliocentred three body problem, Eq. 3.5 results to be:

$$\begin{aligned}\mathbf{a}_{\mathrm{Rel},sc} = &-\frac{\mu_E}{|\mathbf{d}|^3}\mathbf{d}\left\{-\frac{4}{c^2}\frac{\mu_{sun}}{|\mathbf{r}|}-\frac{1}{c^2}\frac{\mu_{sun}}{|\boldsymbol{\rho}|}+\left(\frac{|\dot{\mathbf{r}}|}{c}\right)^2+2\left(\frac{|\dot{\boldsymbol{\rho}}|}{c}\right)^2-\frac{4}{c^2}(\dot{\mathbf{r}}\cdot\dot{\boldsymbol{\rho}})-\frac{3}{2c^2}\left[\frac{\mathbf{d}\cdot\dot{\boldsymbol{\rho}}}{|\mathbf{d}|}\right]^2\right\}+\\ &-\frac{\mu_{sun}}{|\mathbf{r}|^3}\mathbf{r}\left\{-\frac{4}{c^2}\frac{\mu_E}{|\mathbf{d}|}-\frac{1}{c^2}\frac{\mu_E}{|\boldsymbol{\rho}|}+\left(\frac{|\dot{\mathbf{r}}|}{c}\right)^2\right\}+\\ &+\frac{1}{c^2}\frac{\mu_E}{|\mathbf{d}|^3}\left\{\mathbf{d}\cdot[4\dot{\mathbf{r}}-3\dot{\boldsymbol{\rho}}]\right\}\dot{\mathbf{d}}+\frac{1}{c^2}\frac{\mu_{sun}}{|\mathbf{r}|^3}\left\{\mathbf{r}\cdot 4\dot{\mathbf{r}}\right\}\dot{\mathbf{r}}\end{aligned} \tag{3.6}$$

Where $\mathbf{r}$ and $\mathbf{d}$ are the position vectors of the spacecraft with respect to the Sun and Earth respectively, and $\boldsymbol{\rho}$ is the position of Earth with respect to the Sun. The last two terms are a compacted form of the following relations [26]:

$$\frac{1}{2c^2}\sum_{j\neq i}\frac{\mu_j}{r_{ij}^3}(\mathbf{r}_j-\mathbf{r}_i)[\mathbf{r}_j-\mathbf{r}_i]\cdot\ddot{\mathbf{r}}_j \quad \text{and} \quad \frac{7}{2c^2}\sum_{j\neq i}\frac{\mu_j}{r_{ij}}\ddot{\mathbf{r}}_j \tag{3.7}$$

In this context it becomes:

$$\frac{1}{2c^2}\left[\frac{\mu_{\mathrm{E}}}{|\mathbf{d}|^3}(-\mathbf{d})(-\mathbf{d})\cdot\ddot{\boldsymbol{\rho}}\right] \quad \text{and} \quad \frac{7}{2c^2}\left[\frac{\mu_{\mathrm{E}}}{|\mathbf{d}|}\ddot{\boldsymbol{\rho}}\right] \tag{3.8}$$

3.3.1. Validation of the Relativistic Three-Body Problem

The model presented in section 3.3 can be validated by propagating a set of trajectories using both Newtonian and relativistic formulations. Increasing the velocity of the spacecraft and approaching relativistic speeds (i.e. increasing the Lorentz factor γ), the difference between the two propagations should increase as the relativistic effects in the motion become more dominant. The numerical difference between the two models, considering the same initial conditions, can be evaluated using the Mean Squared Error (MSE) as follows:

$$MSE = \frac{1}{N}\sum_{i=1}^{N} d_i^2 \tag{3.9}$$

where where $d_i = ||\mathbf{r_{relativistic,i}} - \mathbf{r_{newtonian,i}}||$ is the norm of the difference of each position vector of the spacecraft along its motion in the two models.

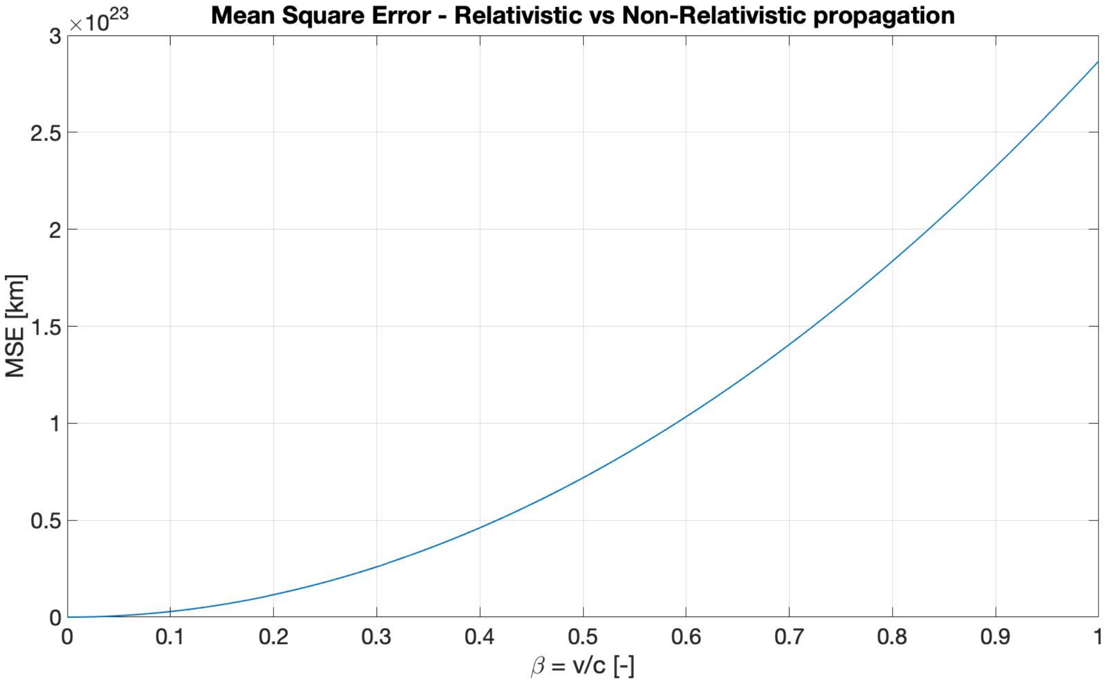

Figure 3.3: MSE computed at different values of β. When $v \ll c$ (i.e., $\beta \to 0$), the Relativistic and Newtonian propagations coincide with no errors, while their difference increases for $\beta \to 1$. The order of magnitude of the MSE is indicative of the lengthy of the propagated trajectory.

The relativistic three-body model can be further validated including the laser acceleration and testing it with various spacecraft properties:

Sail Mass (g)	**Velocity (% c)**	**Lorentz Factor**	**Position Error at Solar System Escape (km)**
0.02	46.2	$\gamma = 1.1279$	8.13×10^5
0.2	32.6	$\gamma = 1.0578$	8.0×10^5
2	20.6	$\gamma = 1.0221$	7.7×10^5
20	12.44	$\gamma = 1.0078$	7.17×10^5
200	7.2	$\gamma = 1.0026$	6.15×10^5
2000	4	$\gamma = 1.0008$	4.62×10^5

Table 3.1: Position error for different sail masses at the solar system exit. The cases shown in this table are model tests and not design choices taken for the trajectory propagation shown in chapter 4. For an equal comparison, the propulsion times are considered sufficiently high to reach high velocities for all the cases, and the reached velocity may differ from other solutions shown in this work.

Table 3.1 demonstrates that within the context of sail acceleration via laser propulsion, the norms of the vectorial differences at Solar System escape increase with rising values of γ.

3.4. Galactic phase

3.4.1. The Oort cloud and the sphere of influence of the Solar System

Defining the boundary of the Solar System is an open field of research in astrophysics, where there's a debate between the definition of such boundary as the volume region within the solar gravitational attraction dominates, and as definition linked to the interaction between the plasma of the solar wind and the interstellar medium [34]. The Oort cloud is assumed to be a vast region of icy planetesimals sorrounding the Solar System, extending between a region of 2000 to 200000 AU from the Sun [28]. Being a really vast region, where the dynamic interactions of the Solar System and the galactic gravitational influences are really complex, its structure is often referred as a inner and outer region [37].

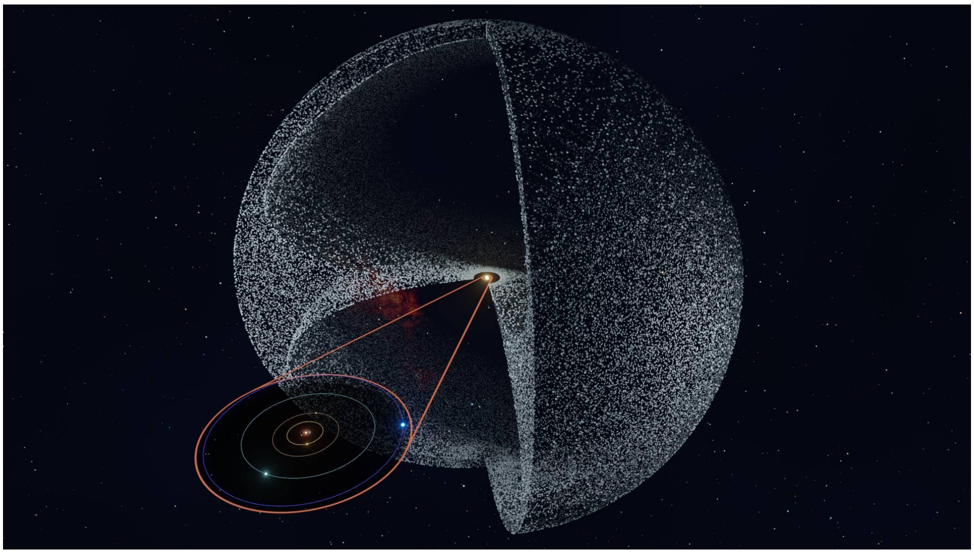

Figure 3.4: An artistic representation of the Oort cloud, not in scale. Copyright: Vito Technology.

However, an analytical approach to determine the Hill Sphere of the Solar System in a galactic stellar disc-Sun-planet system is given by D. Souami (2020) [34], where the sizes of different sphere of influences of the Solar System are evaluated. According to that, the

Hill sphere of the Solar System is estimated as:

$$R_{\text{Hill}} = 0.865\,\text{pc} \approx 178424\,\text{AU} \tag{3.10}$$

In the trajectory propagation, this will be considered as the boundary beyond which the gravitational influence of the galaxy will start acting on the spacecraft. Of course this is an assumption, made to try a novel approach to interstellar mission design discussed earlier, segmenting the mission in phases with dominant bodies inside them. In reality, the transition from a region where the Sun (or the entire Solar System) is dominant to a region where the galactic forces prevail, would be gradual and more complex than this case.

3.4.2. Galactic model

The model described in the section above governs the motion of the spacecraft within the Solar System gravitational influence. Beyond the distance of R_{Hill} from the Sun, the Sun's gravitational influence is no longer dominant. During this phase the spacecraft trajectory is modelled as as point of mass [10] under the Galactic potential model described in Irrgang et al. (2013) [18] with the following equations of motion:

$$\ddot{x} = G\left(-\frac{x \cdot M_b}{(R^2 + b_b^2)^{3/2}} - \frac{x \cdot M_d}{(x^2 + y^2 + (a_d + \sqrt{z^2 + b_d^2})^2)^{3/2}} - \frac{x \cdot M_h}{a_h \cdot R \cdot (a_h + R)}\right), \tag{3.11a}$$

$$\ddot{y} = G\left(-\frac{y \cdot M_b}{(R^2 + b_b^2)^{3/2}} - \frac{y \cdot M_d}{(x^2 + y^2 + (a_d + \sqrt{z^2 + b_d^2})^2)^{3/2}} - \frac{y \cdot M_h}{a_h \cdot R \cdot (a_h + R)}\right), \tag{3.11b}$$

$$\ddot{z} = G\left(-\frac{z \cdot M_b}{(R^2 + b_b^2)^{3/2}} - \frac{z \cdot M_d \left(a_d + \sqrt{z^2 + b_d^2}\right)}{\left(\sqrt{z^2 + b_d^2}\right)\left(x^2 + y^2 + (a_d + \sqrt{z^2 + b_d^2})^2\right)^{3/2}} - \frac{z \cdot M_h}{a_h \cdot R \cdot (a_h + R)}\right). \tag{3.11c}$$

In the equations above, there are constants related to the bulge, disk and halo components of the Galaxy, as well as the Galactocentric spherical radius R defined as:

$$R = \sqrt{r^2 + z^2} \tag{3.12}$$

where

$$r = \sqrt{x^2 + y^2} \tag{3.13}$$

represents the cylindrical coordinate in the plane of the Galaxy, and x, y, z are the position of the point of mass (the spacecraft) in a Galactocentric reference frame. These equations describe the motion of a point of mass under the potential described in Piotr A. Dybczy´nski, Filip Berski (2015) [10] in a Galactocentric frame. The units involved are solar masses $M_\odot$, parsec [pc] and million years [Myr]; with these units the Gravitational constant is in $[pc^3/(M_\odot Myr^2)]$. A more detailed description of the potential is reported in Appendix B. Numerical parameters for this model are taken from [18] and summarized in the following table:

Parameter	**Value**
Distance of the Sun from the Galactic Centre R	8400 pc
Galactic bulge mass Mb	9.51×10^9 $M_\odot$
Galactic disc mass Md	66.4×10^9 $M_\odot$
Galactic halo mass Mh	23.7×10^9 $M_\odot$
Bulge characteristic distance b_b	230 pc
Disc characteristic distance a_d	4220 pc
Disc characteristic distance b_d	292 pc
Halo characteristic distance a_h	2562 pc
Galactic halo cut-off parameter	200000 pc
Galactic halo exponent parameter γ	2
Galactic disc matter density near the Sun ρ_o	0.102 $M_\odot$ pc^{-3}
Galactic rotational velocity of the LSR v_o	242 km s^{-1}

Table 3.2: Numerical parameters of the Galactic model from [18].

3.4.3. Validation of the Galactic model

To validate the implementation of the Galactic potential model, the numerical propagation is compared with existing data extracted from StePPeD 3.3 data release[1] containing numerical ephemerides providing Galactocentric positions of the Sun for the future 30 million years, using the same Galactic potential model described in section 3.4.2. Propagating in MATLAB the orbit of the Sun with the initial conditions $\mathbf{R_{sun}} = (-8400, 0, 17)$ pc and $\mathbf{V_{sun}} = (11.3520, 260.0110, 7.41)$ pc/Myr [10]:

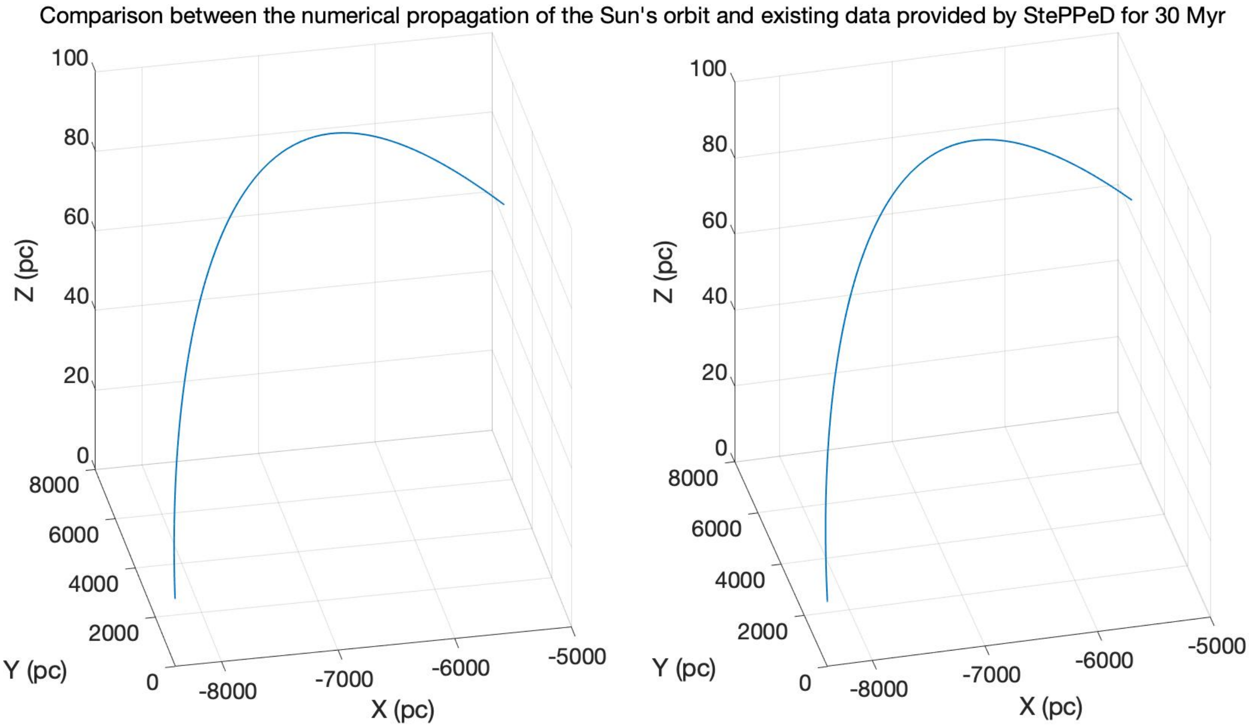

Figure 3.5: Comparison of the orbit propagations of the Sun for a span of 30 million years using Irrgang (2013) potential galactic model [18] using the numerical integration on MATLAB (left plot) and the StePPeD 3.3 data release (right plot)

The numerical propagation of the Sun's orbit and the plot of the ephemerides extracted from the StePPeD 3.3 data release coincide, showing that the Galactic potential model has been implemented correctly.

3.4.4. Arrival

When the spacecraft enters the sphere of influence of Proxima Centauri, the star's gravitational influence becomes dominant and must be taken into account. The dynamics during this phase are not addressed in this work, as they require a profound knowledge of the environment of another Solar System in terms of interplanetary medium, plasma interaction, and other complex phenomena. The star's gravitational influence would equal that of the galaxy's at very small distances from the star (compared to the entire interstellar travel), due to the star's small mass, according to the models used in this work. Proxima Centauri is the smallest star in the Alpha Centauri triple system, and its orbit lies a considerable distance from the barycenter with a semi-major axis of a nominal value of 8700 AU, while Alpha Centauri A and Alpha Centauri B orbit close to the barycenter [20]. In an approach like the one presented in this work, a spacecraft targeting Proxima Centauri would primarily be subject to its gravitational influence, as it would travel a considerable distance from the other system's stars. In practice, the overall modeling of the arrival phase is more complex and warrants further investigation into all environmental aspects, along with the gravitational description.

3.5. Interplanetary and Interstellar mediums disturbances

3.5.1. Interplanetary and Interstellar dust and particles

In this work, gravitational disturbances deviate the spacecraft during its motion, requiring an optimal pointing solution to reach the target. However, interplanetary and interstellar environments are really complex and the interaction with the sail can have multiple effects, here are just reported for completeness, however not treated nor modeled in the trajectory propagation. Interplanetary medium (IPM) and Interstellar medium (ISM) are the whole of all the matter between planets within a solar system and between stars.These can have various origins; in the solar system, the dusts originate from meteoroids, asteroids and comets [15], while in the interstellar field most of the dusts and gases are produced from stellar outflows, planetary nebulae, novae and supernovae [15]. Sizes and densities of such dusts and particles vary depending on the environments and often there's a lot of uncertainty. During the sail's travel, the presence of particles like dust grains, molecular and atomic gases and bigger grains represent a fundamental aspect. The interplanetary medium plays a role especially during the acceleration phase. The solar system dust cloud is mainly shaped around the ecliptic plane [30] where the dust grains span a range of sizes with the peak mass flux between 100 and $400\mu m$ [23]. The impact with grains with size $> 1mm$ would destructive for the spacecraft. Statistical estimates of grain impacts suggest that cumulative exposure could result in significant material degradation and course deviation, contingent upon the velocity vector and sail orientation. Energy transfer considerations, predicated on the kinetic parameters of the dust particles, highlight the need for robust shielding to avert potential compromise to structural integrity. Moreover, the momentum imparted by dust collisions, even though is minimal relative to the spacecraft's total momentum, requires careful assessment to ensure precise navigation. One mitigation solution is to reduce the spacecraft cross section by re-orientation of the sail as shown in figure !!!!. Long term effects on the spacecraft however need more comprehensive research in the field of relativistic grain impacts on a spacecraft [23].

3.5.2. Electromagnetic galactic forces

Another interaction with the interstellar medium is represented by electromagnetic forces caused by the Interstellar magnetic field [16] The spacecraft, when charged by interstellar particles and photons, experiences various forces and torques that can significantly influence its trajectory and structural integrity during interstellar travel. One significant effect of this charging is the deflection of the spacecraft from a straight trajectory due to the interstellar magnetic field. The magnitude of this deflection is dependent on the speed and magnetic field strength and, considering the interaction of a gas column along a 4.42 light years path, can potentially exceed 20 Earth radii. Other physical phenomena involving the Interstellar magnetic field can cause oscillations and rapid spinning of the spacecraft around the axis perpendicular to the direction of motion [16].

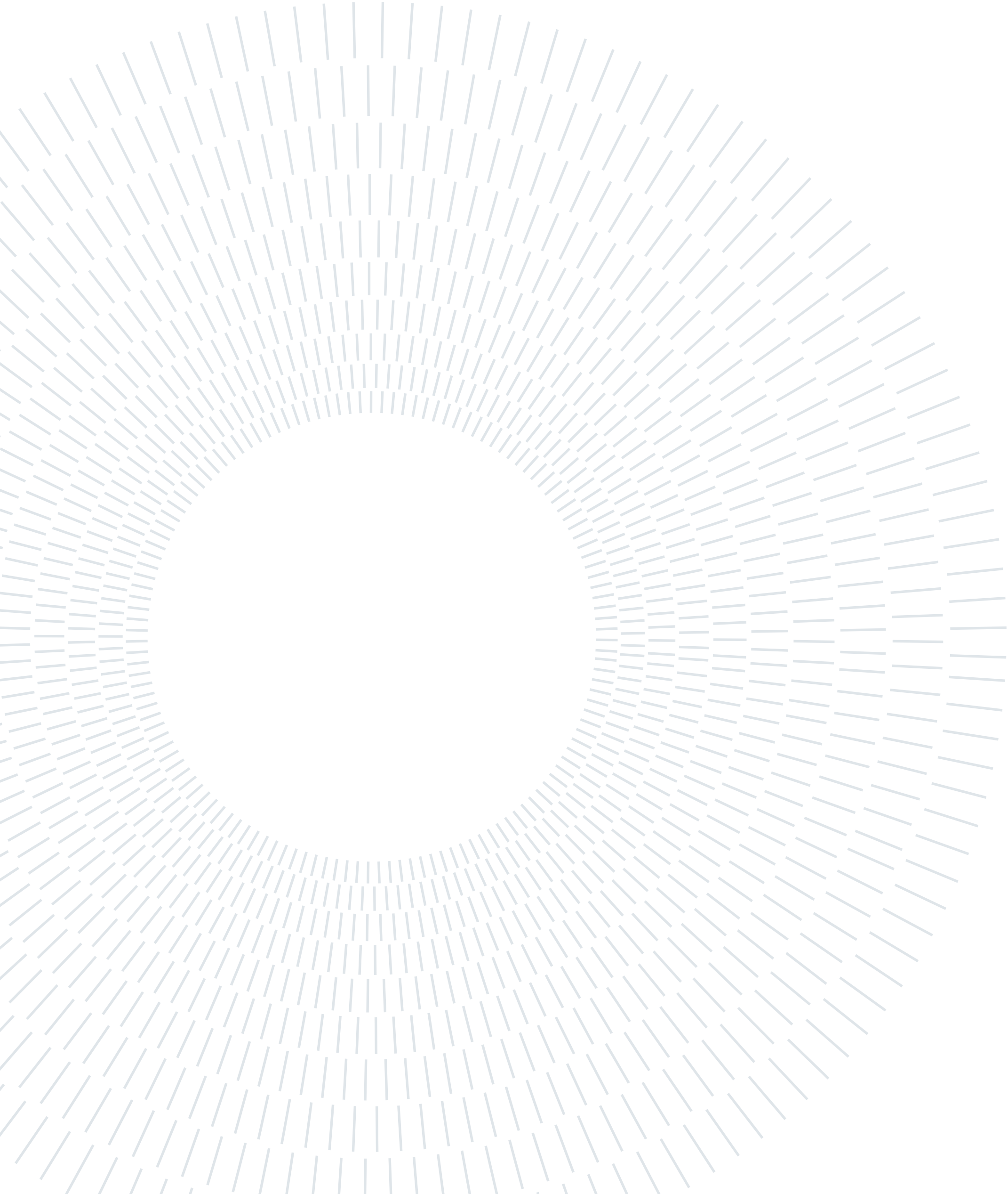

4 | Trajectory propagation

In this chapter the propagation of the trajectory using the gravitational models discussed in Chapter 3 is simulated. As a first approach, the optimal direction of acceleration will be estimated taking into account the gravitational perturbations along the travel, and a further step will consist on the sensibility analysis of such optimal direction introducing gaussian errors at the beginning of the trajectory.

4.1. Optimal acceleration direction

To give an idea of the order of magnitude of the deviation of the spacecraft during its motion, a propagation is performed laser-propelling the spacecraft aiming perfectly to the target direction of Proxima Centauri in the case of $m_{sail} = 1$ g

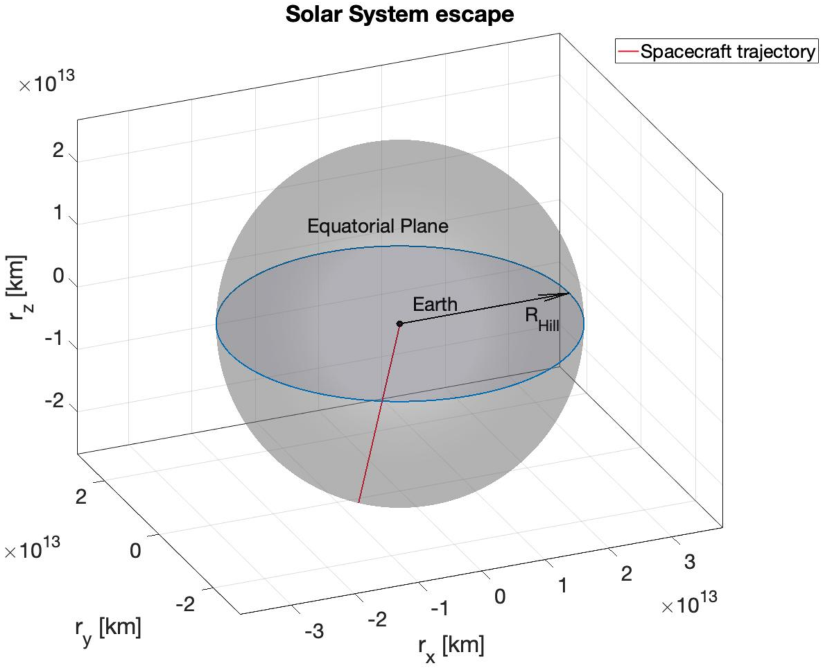

Figure 4.1: Spacecraft trajectory from Earth to the boundary of the Solar System represented by the Hill sphere radius, Earth Centred equatorial frame.

As discussed earlier the trajectory looks rectilinear, as the deflection is so small that is not visible in a large scale. However, the deflection induced by gravity can be monitored as:

$$\epsilon = \cos^{-1}\left(\frac{\hat{\mathbf{r}} \cdot \mathbf{dir}}{\|\mathbf{dir}\|}\right) \tag{4.1}$$

where $\hat{\mathbf{r}}$ and $\mathbf{dir}$ represent respectively the direction of the position vector of the spacecraft at each time instant and the target direction in a geocentric equatorial frame.

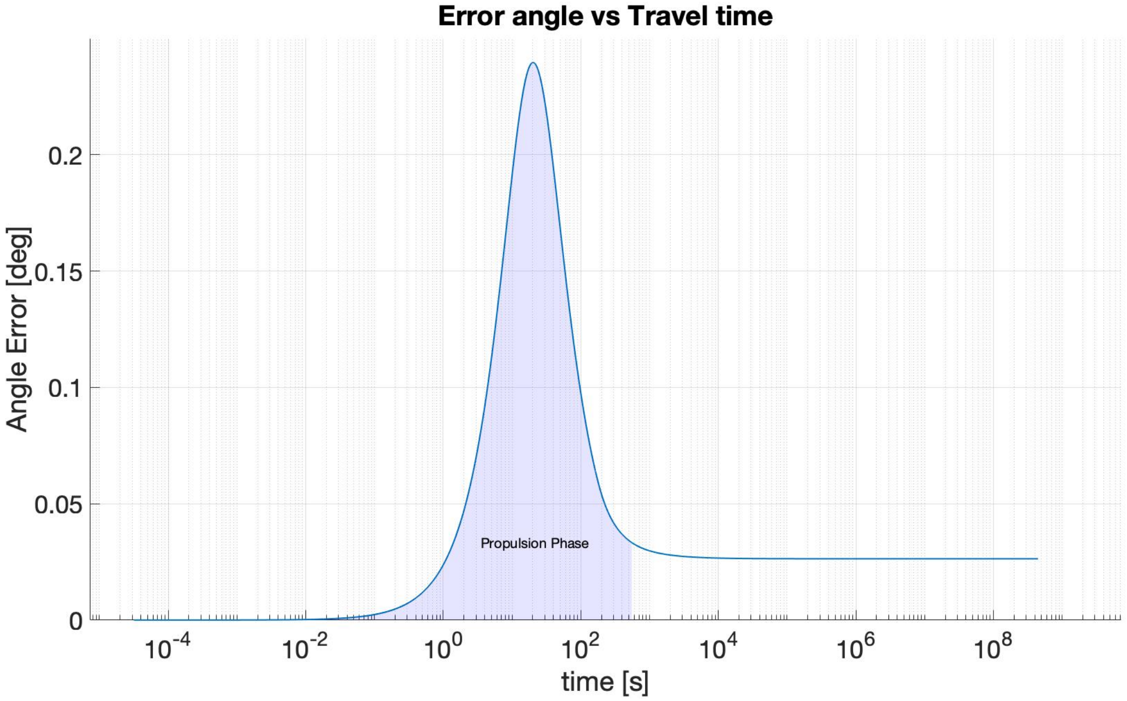

Figure 4.2: Angle error during the travel to the boundary of the Solar System. The plot is semilog plot in the x axis. The highlighted area is intended to represent the time span where the laser propulsion is acting on the spacecraft.

As depicted in the figure above, the error in direction peaks at approximately 0.25 degrees during the acceleration phase and eventually stabilizes. This behaviour reflects the fact that the spacecraft is accelerated from a parking orbit, and its velocity is gradually reoriented towards Proxima Centauri, causing this transitory behaviour. After this transient phase, the spacecraft will tend to align to the target direction. However, the gravitational forces exerted by Earth and the Sun will cause a permanent deviation from the nominal trajectory, in this case, on the order of approximately 0.024 degrees. Such a minor error in relation to the target direction, when extrapolated over the entire mission duration, would result in the spacecraft deviating hundreds of AUs from the target. Specifically, at the boundary of the Solar System, the distance error from the ideal nominal trajectory would be around 82 AU, and considering the entire trajectory, the spacecraft would miss Proxima Centauri by about 338 AU. Although these figures are qualitative estimates derived from simplified models, they highlight the significant impact that even small navigational errors, on the order of arcseconds, can have over vast interstellar distances. Checked the impact on the miss distance by acceleration of the spacecraft towards Proxima Centauri, to optimize the direction of acceleration an objective function is defined, that includes the whole gravitational perturbations and the function to be minimized is the miss distance at the target. The output from the minimization process is the direction vector of laser acceleration expressed in right ascension and declination coordinates, and here reported:

Coordinate	**Mission Case 1** 21.2 years	**Mission Case 2** 37.2 years	**Mission Case 3** 84.8 years
α_{optimal} [deg]	217.187	217.007	216.778
δ_{optimal} [deg]	-62.673	-62.676	-62.626

Table 4.1: Optimal pointing coordinates for the acceleration phase expressed in right ascension and declination in the different mission cases.

In the next section, the sensitivity of this solution will be analyzed, to give estimates of the impact of initial errors during the acceleration phase.

4.2. Sensitivity analysis

In the previous section, the optimal direction of acceleration was found to minimize the miss distance objective function. Further investigation can reveal how errors during the laser acceleration phase impact the overall mission, particularly considering the spacecraft's ability to perform small trajectory corrections to reach the target. The complexity of such a mission is so high that multiple factors could lead to mission failure. However, the probabilities of mission success can be increased by employing a swarm of laser sails, a strategy proposed by the Breakthrough Starshot project [14]. This strategy is the starting point here; a set number of $N = 1000$ sails is considered, with each sail characterized by different initial conditions and a unique set of errors. The considered sources of errors are:

- **Pointing errors**: the laser beam aims to directions misaligned with respect to the optimal direction.
- **Initial state errors**: random dispersions around the nominal initial position in the parking orbit $\mathbf{r_0}$ are introduced.

- **Boosting time errors**: according to different boosting times, the spacecraft would be brought to different positions and different velocities.

A normal gaussian distribution is considered for the errors with the following standard deviations:

Variable nominal value	**Standard deviations σ**
$\alpha_{optimal}$	0.01 - 1 [deg]
$\delta_{optimal}$	0.01 - 1 [deg]
time$_{propulsion}$	0.01 - 1 [s]
Initial position vector orientation	0.01 - 1 [deg]

Table 4.2: The column of the standard deviations shows a range of standard deviations used to propagate the trajectories. The assumed values do not reflect real standard deviations in a real mission scenario but are arbitrary values.

While the variables α, δ, time$_{propulsion}$ are related to the propulsion process, the last variable represents the spacecraft initial position in its parking orbit, expressed in angular orientation with respect to the initial nominal $\mathbf{r_0}$ position of the spacecraft, described in Section 3.2 , Equation 3.1, in the parking orbit's plane. As a first approach, a uniform standard deviation value can be used for all the variables. A further investigation can be performed to understand the sensitivity of the trajectory propagation to a specific variable variation. Starting from a uniform standard deviation of 0.01 degrees and seconds, the propagations of 1000 spacecrafts lead to the following dispersion around Proxima Centauri:

Case 1: $m_{sail} = 1g$ Travel time : $21.2\,years$

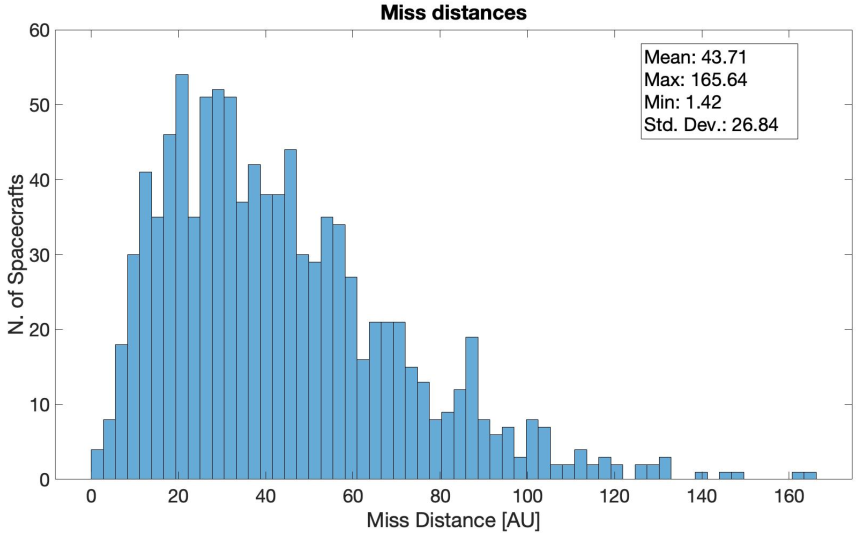

Figure 4.3: Miss distances from Proxima Centauri with 1000 launches with a **0.01 degrees** standard deviation for the pointing and initial position and **0.01 seconds** for the boost time.

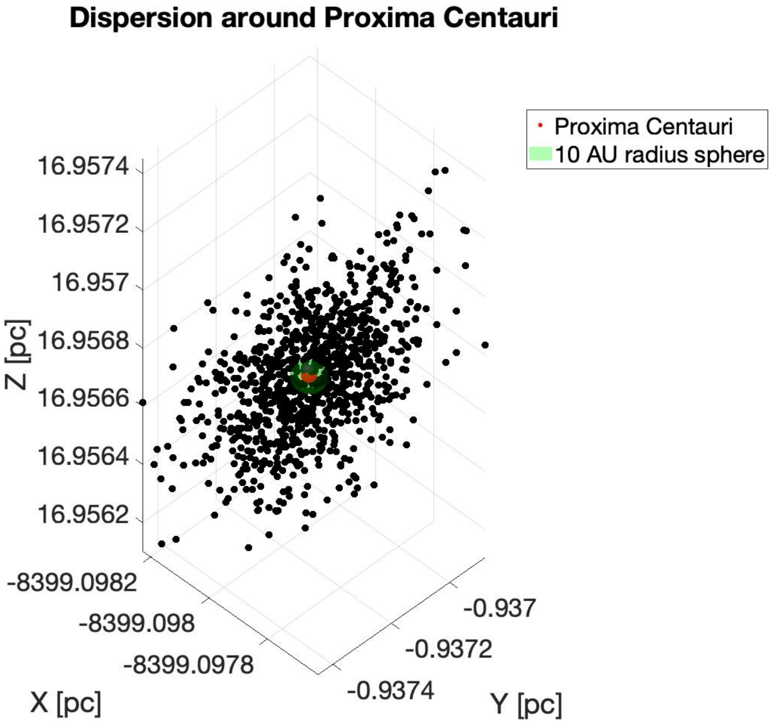

Figure 4.4: Dispersion plot around Proxima Centauri in a galactocentric reference frame. Proxima Centauri (i.e. the centre of its volume error) is not in scale.

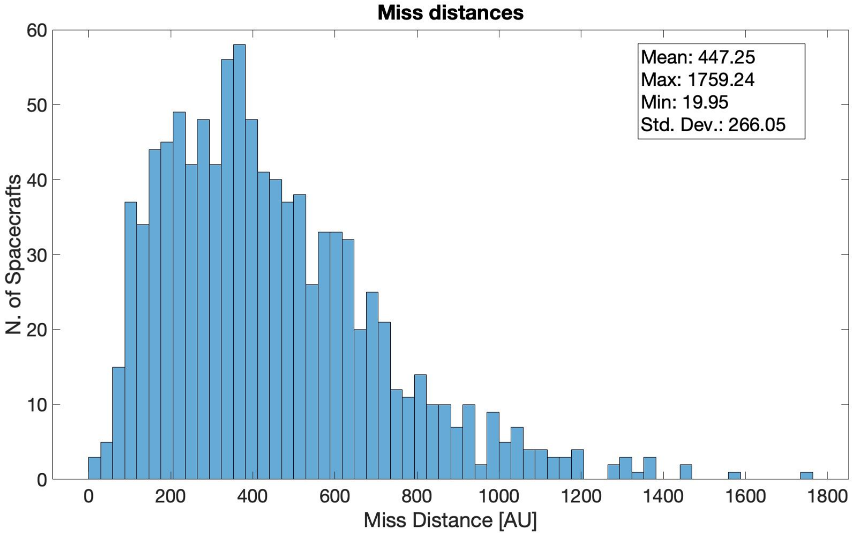

Figure 4.5: Miss distances from Proxima Centauri with 1000 launches with a **0.1 degrees** standard deviation for the pointing and initial position and **0.1 seconds** for the boost time.

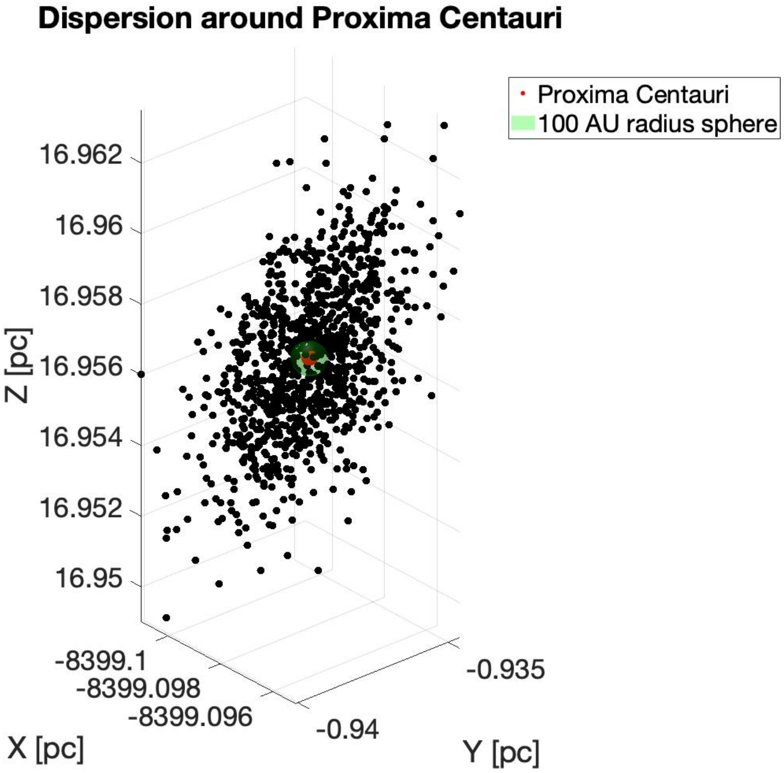

Figure 4.6: Dispersion plot around Proxima Centauri in a galactocentric reference frame. Proxima Centauri (i.e. the centre of its volume error) is not in scale. It's important to note that here the reference sphere is 100 AU radius.

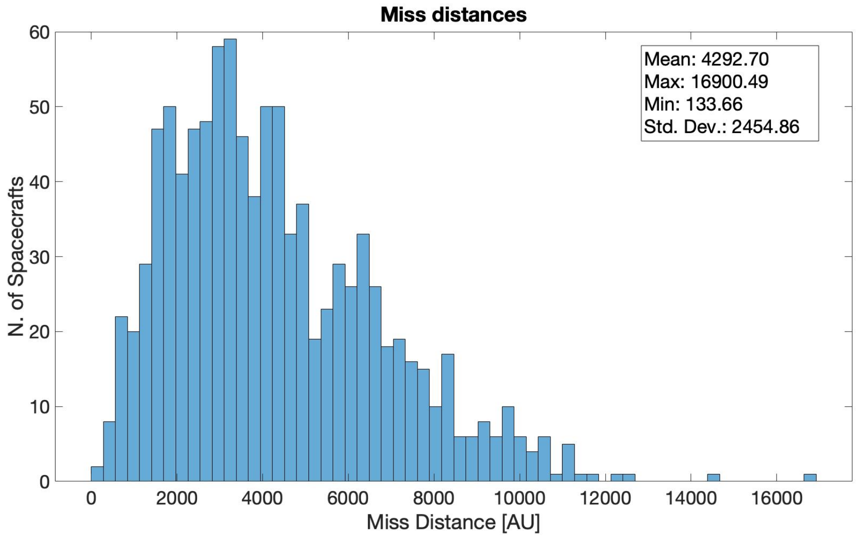

Figure 4.7: Miss distances from Proxima Centauri with 1000 launches with a **1 degree** standard deviation for the pointing and initial position and **1 second** for the boost time.

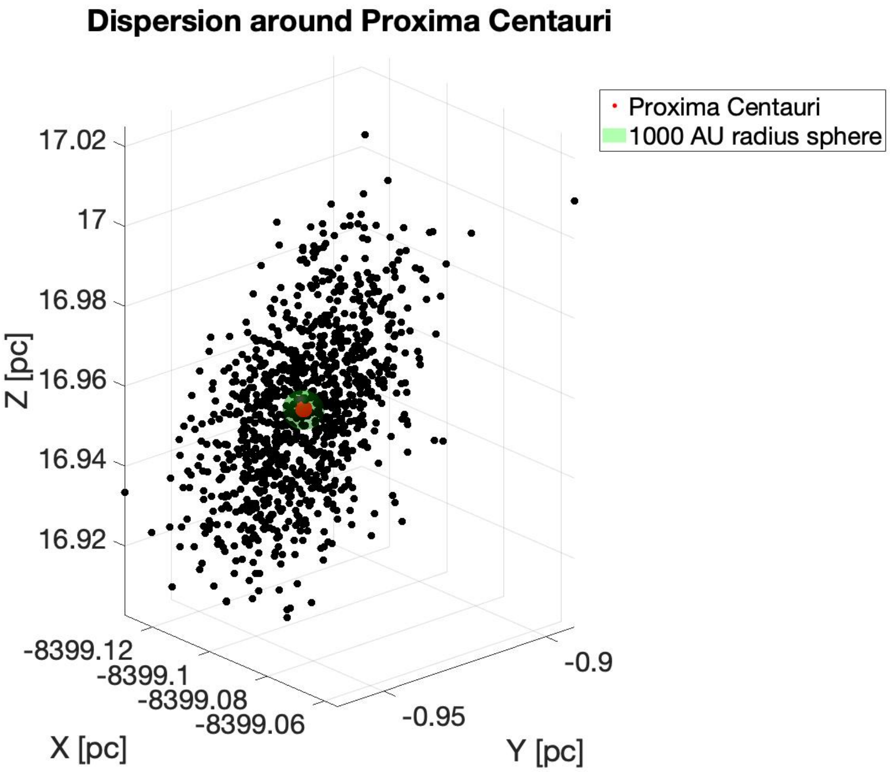

Figure 4.8: Dispersion plot around Proxima Centauri in a galactocentric reference frame. Proxima Centauri (i.e. the centre of its volume error) is not in scale. It's important to note that here the reference sphere is 1000 AU radius.

Case 2: $m_{\text{sail}} = 20g$ Travel time: $37.2\,years$

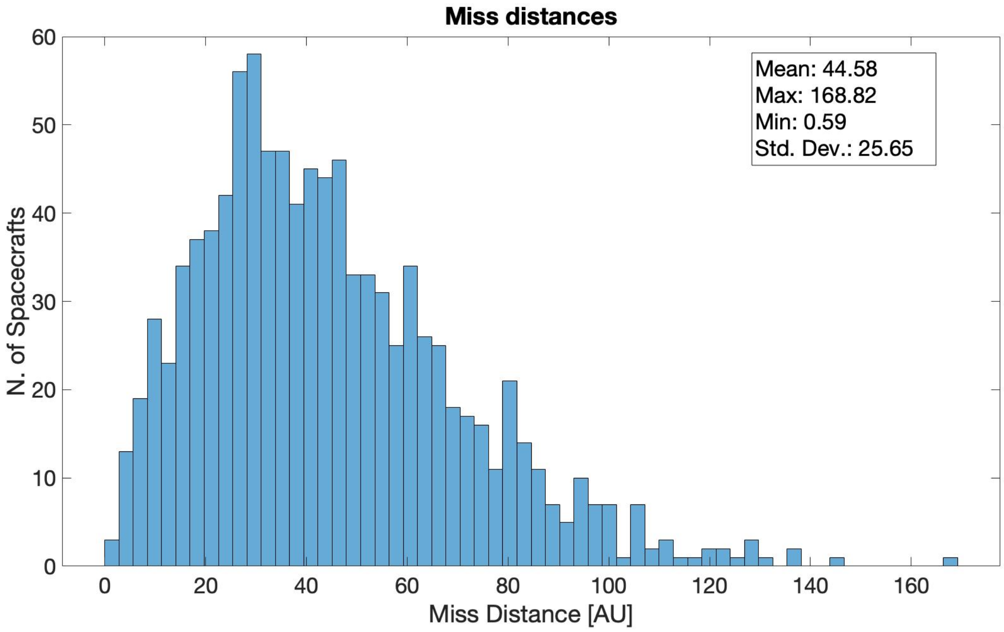

Figure 4.9: Miss distances from Proxima Centauri with 1000 launches with a **0.01 degree** standard deviation for the pointing and initial position and **0.01 second** for the boost time.

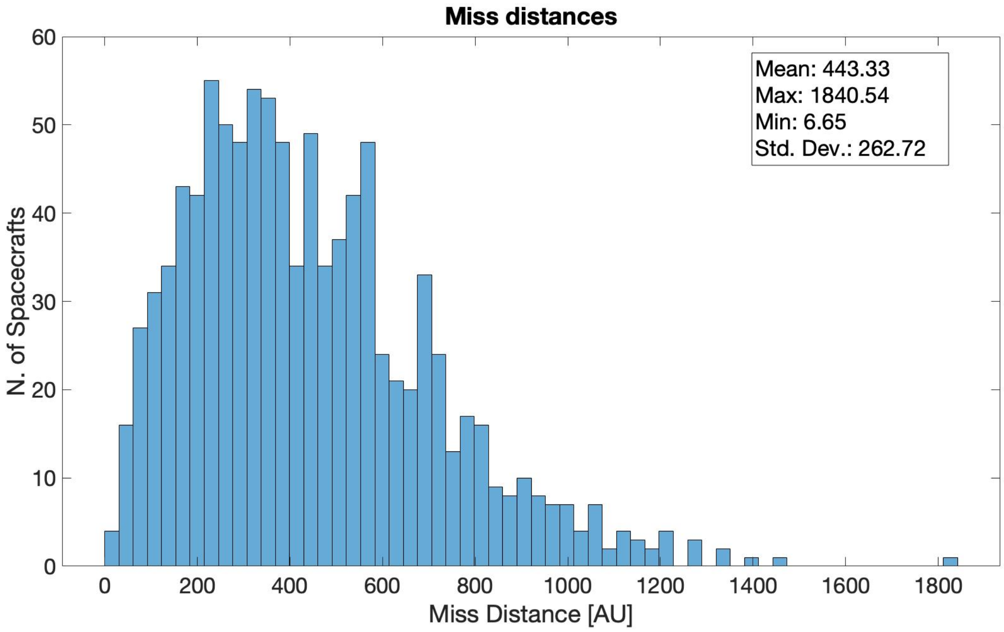

Figure 4.10: Miss distances from Proxima Centauri with 1000 launches with a **0.1 degree** standard deviation for the pointing and initial position and **0.1 second** for the boost time.

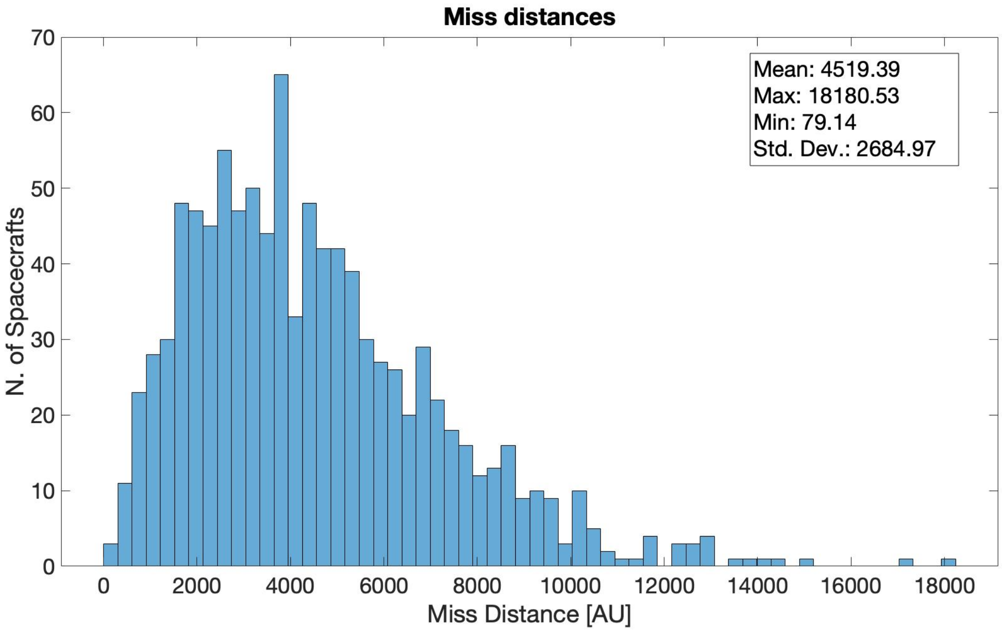

Figure 4.11: Miss distances from Proxima Centauri with 1000 launches with a **1 degree** standard deviation for the pointing and initial position and **1 second** for the boost time.

Case 3: $m_{\text{sail}} = 200g$ Travel time: $84.7\,years$

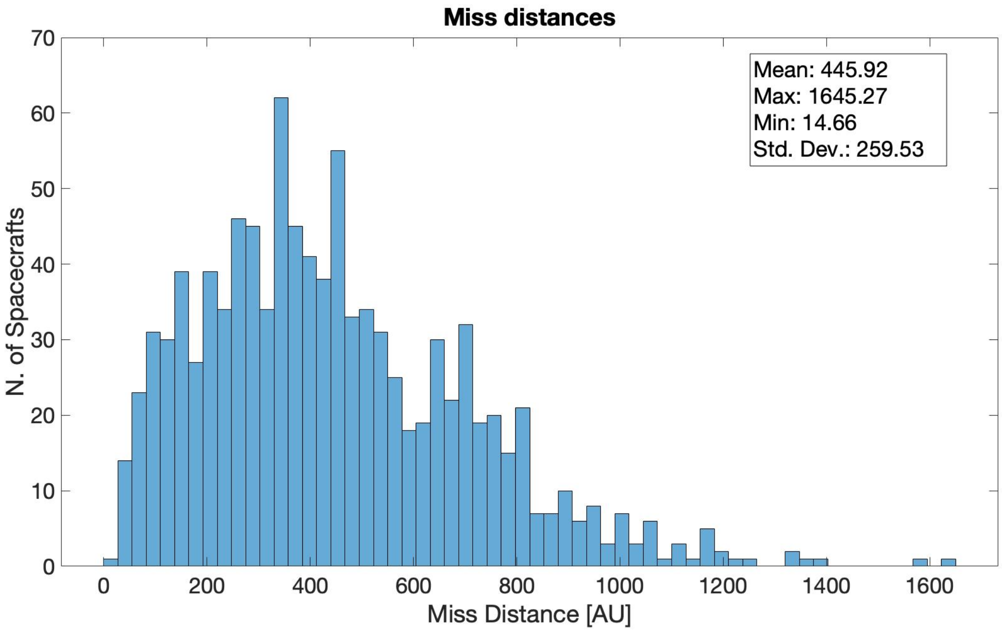

Figure 4.13: Miss distances from Proxima Centauri with 1000 launches with a **0.1 degree** standard deviation for the pointing and initial position and **0.1 second** for the boost time.

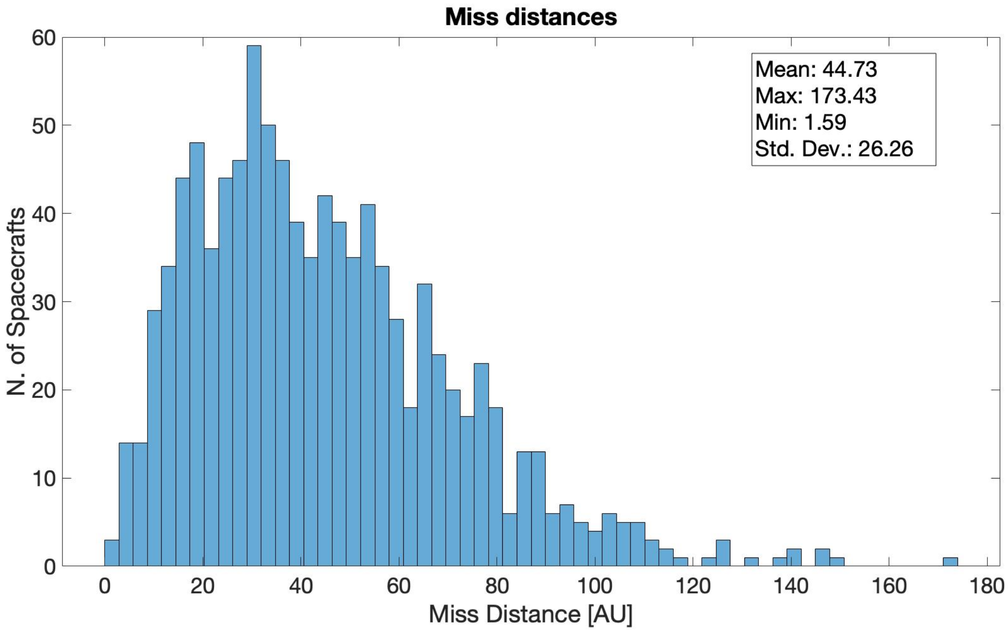

Figure 4.12: Miss distances from Proxima Centauri with 1000 launches with a **0.01 degree** standard deviation for the pointing and initial position and **0.01 second** for the boost time.

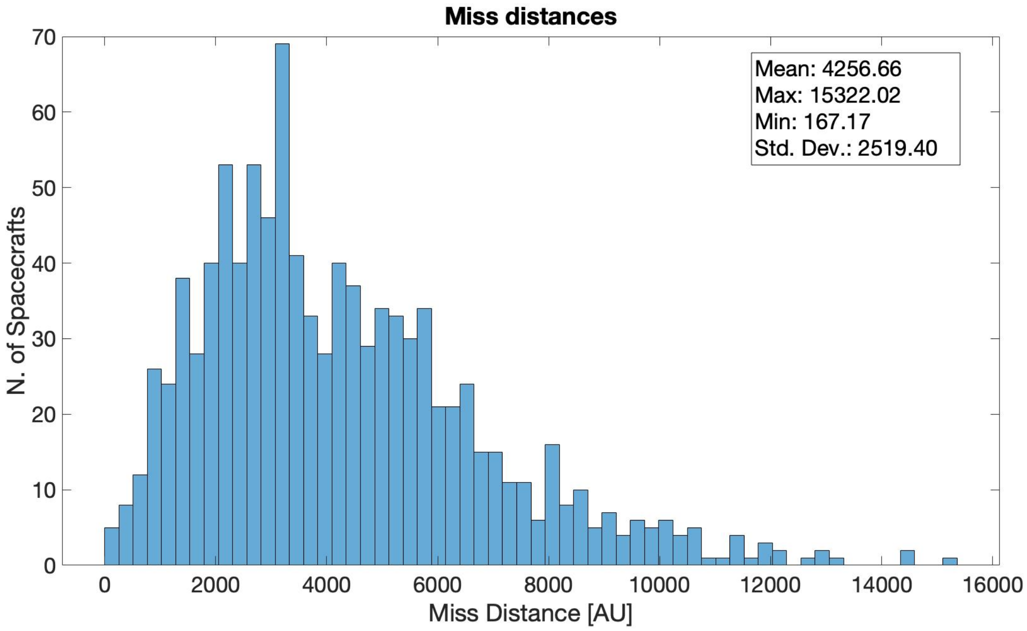

Figure 4.14: Miss distances from Proxima Centauri with 1000 launches with a **1 degree** standard deviation for the pointing and initial position and **1 second** for the boost time.

4.2.1. Analysis of the results

The plot demonstrates that as initial errors are increased by orders of magnitude, the resulting trajectory deviations in simulations also escalate correspondingly. This trend aligns with findings by A. Jackson (2017) [19], despite differences in the error parameters and models, thus precluding direct comparison. Jackson's model is different from the one elaborated in this work, and the same behaviours obtained suggest that segmenting the whole mission in different phases, with a dominant body acting on the spacecraft like in the patched conics method, even in the perspective of future interstellar missions could be a preliminary approach. Consistent with discussions throughout this work, small inaccuracies during the acceleration phase lead to substantial miss distances in the target star system. For instance, with a uniform standard deviation of 0.01 degrees and seconds, the calculated mean miss distance at the target is 43.71 AU. This deviation far exceeds the correctional capabilities of the photon thrusters proposed for this class of spacecrafts, which are estimated to adjust trajectories by approximately 1 AU with 0.3 grams of Pu-238 in a Radioisotope Thermoelectric Generator (RTG) system [23]. According to the model presented here, out of a swarm of 1000 spacecraft, merely an estimated of $\sim 1.5\%$ would reach the target with miss distances of $< 5AU$ for the considered cases of a standard deviation of 0.01 (degrees and seconds) , without in-flight trajectory adjustments. The comparison among the three scenarios, each featuring a different payload mass, reveals no significant discrepancies in trajectory deviations. The extent of trajectory errors and the magnitude of miss distances are more heavily influenced by the initial errors rather than by the mass of the spacecraft. Nonetheless, an increase in payload mass may enhance the spacecraft's capability for trajectory adjustments. This comes at the cost of reduced achievable velocity and extended travel times, presenting a trade-off. Focusing on Case 1, different tests can be conducted to determine which source of error has the predominant impact on trajectory deviations.

By calibrating the initial errors to include only boosting time errors (0.01 seconds) in one instance and only initial position orientation errors (0.01 degrees) in another, we find that the impact on miss distances is approximately 10^{-3} AU for each scenario. However, when considering solely pointing errors (again 0.01 degrees), the miss distances increase to the order of tenths of AU. As it might be expected then, pointing errors during the acceleration phase have the highest effect on trajectory errors hence on the mission success. A primary concern of a trajectory of this kind is to reduce as much as possible pointing errors, rotating the laser beam according to the measured errors during the propulsion phase. Nonetheless, errors in boost times or initial spacecraft positions are also significant, as even miss distances ranging from 10^{-3} to 1 AU require in-mission adjustments, revealing their critical impact.

It would be insightful to identify the threshold below which most launches successfully reach the target within a ’safe’ region, which can be defined as a miss distance of less than 3 AU. Defining a safe region to evaluate the mission’s success in terms of trajectory is complex, as it involves a combination of the spacecraft’s ability to perform minor trajectory corrections and the trajectory deviations arising from various sources. As previously mentioned, Lubin [23] provides an estimate of possible trajectory adjustments of up to 1 AU, considering the electrical and thermal components of thrust from an onboard RTG with 0.3 grams of Pu-238 over an approximately 20-year mission. Even if the pointing errors were null, electromagnetic forces exerted by the interstellar magnetic field would generate trajectory displacements of around 0.1 AU. Therefore, the allowable trajectory corrections related to gravitational disturbances should be less than 1 AU, according to this qualitative estimation. However, considering the model’s simplifications and potential advancements in trajectory modification, a small margin is assumed, and the safe region is set to less than 3 AU. High-resolution cameras and sensors could potentially expand this region, as they would still collect data even at greater distances from the target and the exoplanet orbiting the star.

Defined the success threshold of the mission in terms of miss distance from the target, different values of σ can be tested to estimate the success rate on a swarm of 1000 spacecrafts. However, the introduced errors are gaussian distributed and the outcomes of the simulations in terms of dispersions around the target may vary from a simulation to another. To be statistically consistent, the success rate for a given σ needs to be evaluated as the mean of the success rate outcomes obtained with the same errors conditions. For this purpose, only pointing errors are considered as they represent the dominant source of trajectory deviations, in a range of $\sigma = 0.0001$ - 0.01 degrees, reported in the following table in arcseconds:

σ_{pointing} [arcsec]	Mean Success Rate (Miss distance $<$ 3 AU)
36	0.53%
28.8	0.67%
21.6	1.07%
18	1.53%
10.8	4.33%
7.2	9.77%
3.6	35.04%
2.88	47.15 %
2.16	64.9 %
1.8	74.5 %
1.08	95.71 %
0.72	99.4 %
0.36	100 %

Table 4.3: Mean success rates for various standard deviations of the pointing errors. The success rate is defined as the fraction of spacecrafts that intercepts the target with a miss distance smaller than 3 AU. The simulations are performed for 1000 launches.

Of course this represents a simplified evaluation since the success of the mission isn't given only by making sure that the spacecraft reaches the target from a trajectory standpoint, but there are multiple factors that can lead a single spacecraft to failure. However, table 4.3 shows that in order to approach a reasonable success rate, pointing errors in the order of $0.36 - 1$ arcseconds should be, as results of this particular model, the requirements in terms of pointing accuracy using the laser propulsion system. In particular, for $\sigma_{pointing} = 0.36$ arcseconds, all the simulations give arrivals within 3 AU from Proxima Centauri, and a rate of 96.7% considering a miss distance of 1 AU.

4.3. Feedback control for the laser beam during the acceleration phase

Recognizing the importance of maintaining the spacecraft's direction with high accuracy, an additional approach could be to use a movable, rather than static, laser beam to minimize pointing errors as much as possible. Assuming again Gaussian distributed errors in the initial laser beam direction, a proportional–integral–derivative controller (PID controller) algorithm is used to reduce the errors between the actual position of the spacecraft and the optimal direction obtained in the optimization process shown in section 4.1. It's important to note that this procedure is highly simplified and it's a preliminary approach to the control problem. In general, the output for a PID controller is given by:

$$u(t) = K_p e(t) + K_i \int_0^{t_{prop}} e(\tau) d\tau + K_d \frac{de(t)}{dt} \tag{4.2}$$

where K_p and K_i are respectively the proportional and the integral gain, and K_d is the derivative gain. Equation 4.2 is the general analytical expression while in this case a discrete approach is implemented in MATLAB, and $\mathbf{e(t)}$ represents the error vector between the position of the spacecraft at each time step and the optimal direction:

$$\mathbf{e(t)} = \hat{\mathbf{r_{opt}}} - \hat{\mathbf{r(t)}} \tag{4.3}$$

and the output $\mathbf{u(t)}$ is a vector that steers the laser beam to align the spacecraft with the optimal direction.

$$\mathbf{a_{laser,controlled}(t)} = \mathbf{a_{laser}(t)} + \mathbf{u(t)} \tag{4.4}$$

By introducing a pointing error with a standard deviation of $\sigma_{pointing} = 0.01$ degrees, we can observe how the spacecraft is accelerated in the following figure:

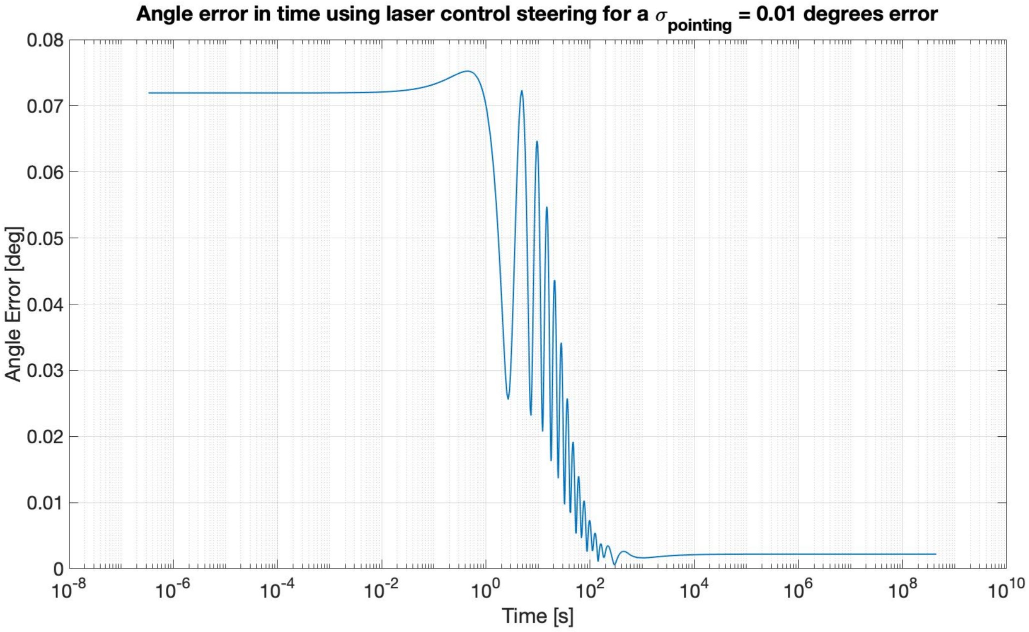

Figure 4.15: Error angle between the position of the spacecraft and the optimal target direction with a PID control system acting. $m_{sail} = 1$ g , $t_{propulsion} = 550$ s , with a $\sigma = 0.01$ degrees error in the initial acceleration direction.

The gains must be accurately tuned, as the laser propulsion can rapidly steer the spacecraft's direction of motion. With this control algorithm the spacecraft oscillates around the optimal direction decreasing gradually the error with respect to it, eventually reaching ~ 0.001 degrees pointing errors. Visualizing the steering angles in time of the laser beam while controlling the position of the spacecraft :

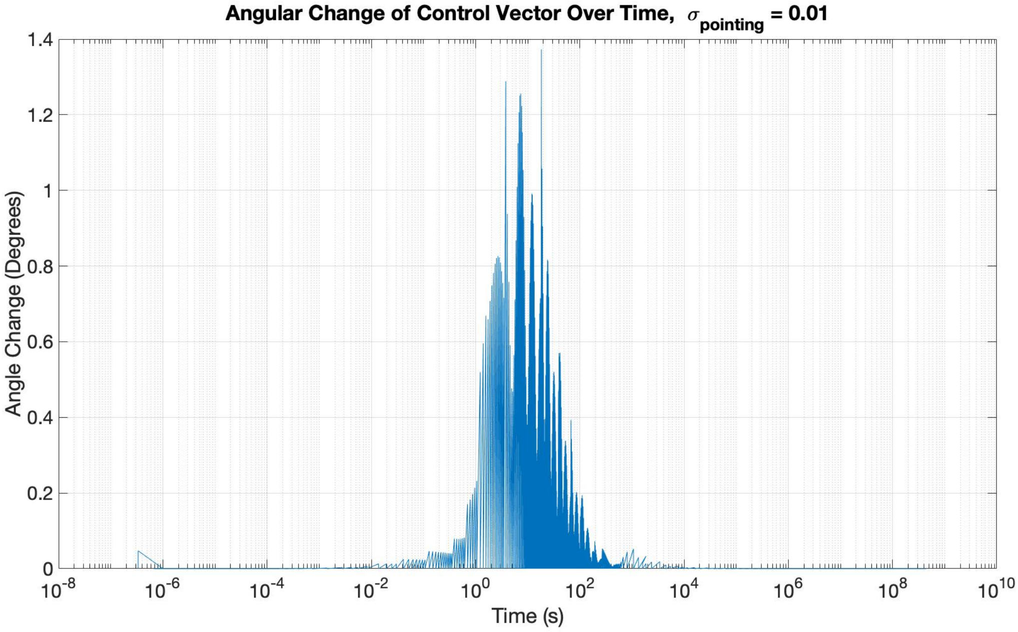

Figure 4.16: Steering angle of the laser beam required to align the spacecraft with the optimal direction, $m_{sail} = 1$ g , $t_{propulsion} = 550$ s, with a $\sigma = 0.01$ degrees error in the initial acceleration direction.

Figure 4.16 shows a peak of ~ 1.4 degrees in the laser beam orientation and a mean of 0.095 degrees during all the propulsion phase. A PID controller might not be the right control algorithm for this purpose, given the complex dynamics involved. However, by introducing a Gaussian error in the initial moments of the acceleration phase, the PID controller is capable of reducing the angular errors, which involve rotations of the laser beam averaging around 0.095 degrees.

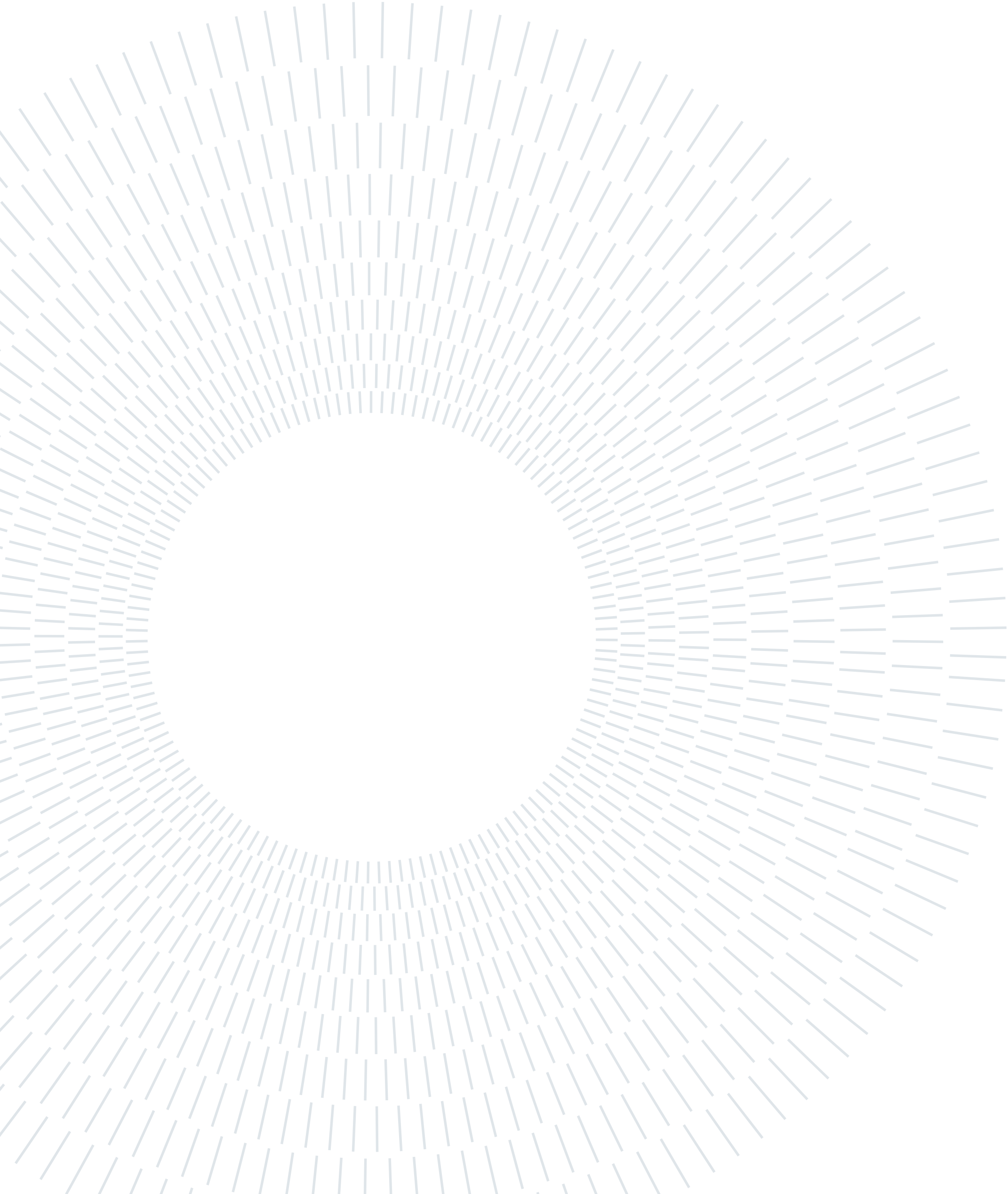

5 | Conclusion

The simulation of interstellar travel necessitates extensive expertise across various domains to execute an accurate numerical model that authentically reproduces reality. The assumptions and simplifications employed in this study elucidate that such a mission demands further inquiry and examination, nevertheless the model has been developed while preserving a scientific and engineering-oriented methodology. The implemented models simulate the dynamics of a spacecraft propelled by a laser beam using a laser DE-STAR system, estimating the gravitational perturbations encountered during the mission. Propelling a spacecraft to 20% of the speed of light without onboard propulsion resembles using a slingshot over an immense trajectory, with uncertainties about the projectile's path deviation while aiming the target. The outcomes of this research underscore the influence of arcsecond-level pointing inaccuracies on trajectory propagation. A dispersion analysis regarding miss distances from the target was conducted for three mission scenarios, each incorporating varying levels of errors during the acceleration phase. Principal findings demonstrate the substantial impact of these errors on the arrival miss distance, highlighting the impracticality of errors ranging from 0.01 to 1 degrees in pointing accuracy, resulting in deviations of tens of thousands of AU from the target. Inverting the question allows for defining the maximal admissible errors to maintain the spacecraft within a safe vicinity of Proxima Centauri, delineated as 3 AU from the target. This analysis concludes that errors with standard deviations of 0.36 arcseconds (10^{-4} degrees) ensure a 100% success rate in all simulations from a trajectory analysis perspective, with an acceptable accuracy range of 0.36 to 1.08 arcseconds. Thus, the laser propulsion system in a real application should be for example capable of orienting the beam to reduce as much as possible initial deviations, that couldn't be corrected in the cruise phase. The results highlight the trajectory's sensitivity to initial pointing errors. A realistic mission scenario, like the Breakthrough Starshot project, consists on deploying a swarm of spacecrafts, launched at regular intervals and communicating their current paths and orientations, thereby minimizing trajectory deviations and optimizing target attainment. Employing laser propulsion and laser sails represents the forthcoming frontier in space exploration. The developmental outcomes of such missions and propulsion systems promise vast benefits, expanding our understanding of proximate stellar systems but also revolutionizing our approach to exploring the solar system and its frontiers.

Bibliography

[1] StePPeD - Stellar Potential Perturbers Database, v. 3.3, 2023. URL `https://pad2.astro.amu.edu.pl/StePPeD/index.php?n=Stars33.Downloads1`. Accessed: 2023-11-22.

[2] G. Anglada-Escudé, P. Amado, J. Barnes, et al. A terrestrial planet candidate in a temperate orbit around proxima centauri. *Nature*, 536:437–440, 2016. doi: https://doi.org/10.1038/nature19106. Received: 06 May 2016, Published: 24 August 2016.

[3] R. R. Bate, D. D. Mueller, and J. E. White. *Fundamentals of Astrodynamics*. Dover Books on Astronomy and Astrophysics. Dover Publications, New York, 1971. ISBN 0486600610.

[4] K. A. Beals, M. Beaulieu, F. J. Dembia, J. Kerstiens, D. L. Kramer, J. R. West, and J. A. Zito. Project longshot: An unmanned probe to alpha centauri. Technical Report NASA-CR-184718, U.S. Naval Academy, 1988. Document ID: 19890007533. Available at: `https://ntrs.nasa.gov/citations/19890007533`.

[5] J. Bible, I. Johansson, G. B. Hughes, and P. M. Lubin. Relativistic propulsion using directed energy. *SPIE Nanophotonics and Macrophotonics for Space Environments*, 8876:887605, 2013. doi: 10.1117/12.2035346.

[6] A. Bond and A. R. Martin. Project Daedalus. *Journal of the British Interplanetary Society*, 31:S5–S7, Jan. 1978.

[7] A. Butkevich and L. Lindegren. 4.1.7 transformations of astrometric data and error propagation. `https://gea.esac.esa.int/archive/documentation/GDR3/Data_processing/chap_cu3ast/sec_cu3ast_intro/ssec_cu3ast_intro_tansforms.html`, 2023. Gaia Data Release 3 Documentation release 1.3, European Space Agency.

[8] G. Collaboration. Gaia early data release 3. the celestial reference frame (gaia-crf3). *Astronomy Astrophysics*, 667:A148, nov 2022. doi: 10.1051/0004-6361/202243483. URL `https://ui.adsabs.harvard.edu/abs/2022A&A...667A.148G`. Provided by the SAO/NASA Astrophysics Data System.

[9] G. Collaboration. How to write adql queries for gaia data - epoch_prop. `https://www.cosmos.esa.int/web/gaia-users/archive/writing-queries/#EpochPropagationFlag`, 2023. Accessed: [inserisci la data di accesso qui].

[10] P. A. Dybczyń ski and F. Berski. On the accuracy of close stellar approaches determination. *Monthly Notices of the Royal Astronomical Society*, 449(3):2459–2471, apr 2015. doi: 10.1093/mnras/stv367. URL `https://doi.org/10.1093%2Fmnras%2Fstv367`.

[11] G. Dyson. *Project Orion: The True Story of the Atomic Spaceship*. Henry Holt and Co., 1 edition, 2002. ISBN 0805059857. Based on the study conducted by United States Air Force, DARPA, NASA in the 1950s and 1960s.

[12] R. L. Forward. Roundtrip interstellar travel using laser-pushed lightsails. *Journal of Spacecraft and Rockets*, 21:187, 1984. doi: 10.2514/3.8632. URL `https://doi.org/10.2514/3.8632`.

[13] GAIA mission, ESA. Gaia data release 3 (dr3). `https://gea.esac.esa.int/archive/`, June 13 2022. Accessed: August 2023.

[14] P. Gilster. Breakthrough starshot: Mission to alpha centauri. *Centauri Dreams. Retrieved 14 April 2016*, 2016.

[15] E. Grün and J. Svestka. Physics of interplanetary and interstellar dust. *Space Science Reviews*, 78(1-2):347–360, 1996.

[16] T. Hoang and A. Loeb. Electromagnetic forces on a relativistic spacecraft in the interstellar medium. *The Astrophysical Journal*, 848(1):31, 2017.

[17] B. initiatives. Breakthrough starshot animation (full), 2016. URL `https://www.youtube.com/watch?v=xRFXV4Z6x8s&t=39s`. Accesso in data 29 novembre 2023.

[18] A. Irrgang, B. Wilcox, E. Tucker, and L. Schiefelbein. Milky way mass models for orbit calculations. *Astronomy & Astrophysics*, 549:A137, Jan 2013. doi: https://doi.org/10.1051/0004-6361/201220540. Number of page(s): 13, Section: Galactic structure, stellar clusters and populations, Published online: 15 January 2013.

[19] A. Jackson. Dispersion analysis of small-scale-spacecraft interstellar trajectories. 2017.

[20] P. Kervella, F. Thévenin, and C. Lovis. Proxima's orbit around centauri. *Astronomy & Astrophysics (A&A)*, 598:L7, February 2017. doi: https://doi.org/10.1051/0004-6361/201629930. Published online: 30 January 2017.

[21] N. Kulkarni, P. Lubin, and Q. Zhang. Relativistic spacecraft propelled by directed energy. *The American Astronomical Society*, 155(4), 2018. doi: 10.3847/1538-3881/aaafd2.

[22] J.-C. Liu, Z. Zhu, and H. Zhang. Reconsidering the galactic coordinate system. *A&A*, 526:A16, Feb 2011. doi: https://doi.org/10.1051/0004-6361/201014961. URL `https://www.aanda.org/articles/aa/abs/2011/02/aa14961-10/aa14961-10.html`. Published online: 14 December 2010.

[23] P. Lubin. A roadmap to interstellar flight. *JBIS*, 69:40–72, 2016. doi: https://doi.org/10.48550/arXiv.1604.01356.

[24] X. Luri, A. Brown, L. Sarro, F. Arenou, C. Bailer-Jones, A. Castro-Ginard, J. de Bruijne, T. Prusti, C. Babusiaux, and H. Delgado. Gaia data release 2-using gaia parallaxes. *Astronomy & Astrophysics*, 616:A9, 2018.

[25] G. Marx. Interstellar vehicle propelled by terrestrial laser beam. *Nature*, 211:22–23, 1966. doi: https://doi.org/10.1038/211022a0.

[26] A. Masat. B-plane orbital resonance analysis and applications. perturbed semi-analytical model for planetary protection and defence applied to ballistic resonant flyby design. Master's thesis. supervisor: Camilla colombo, Politecnico di Milano, Milano, 2019. URL = `https://hdl.handle.net/10589/151660`.

[27] J. Maxwell. *A Treatise on Electricity and Magnetism.* Oxford University press, 1873.

[28] A. Morbidelli. Origin and dynamical evolution of comets and their reservoirs. *arXiv preprint astro-ph/0512256*, 2005.

[29] K. L. Parkin. The breakthrough starshot system model. *Acta Astronautica*, 152:370–384, 2018. doi: 10.1016/j.actaastro.2018.08.035.

[30] A. R. Poppe. An improved model for interplanetary dust fluxes in the outer solar system. *Icarus*, 264:369–386, 2016.

[31] J. L. Redding. Interstellar Vehicle propelled by Terrestrial Laser Beam. *Nature*, 213 (5076):588–589, feb 1967. doi: 10.1038/213588a0.

[32] S. Redfield. The local interstellar medium. `https://sethredfield.wescreates.wesleyan.edu/lism.html`. Accessed: 2023-11-30.

[33] I. Ribas et al. The habitability of proxima centauri b. i. irradiation, rotation and volatile inventory from formation to the present. *Astronomy & Astrophysics*, 596:A111–A129, December 2016. doi: https://doi.org/10.1051/

0004-6361/201629576. URL `https://www.aanda.org/articles/aa/abs/2016/12/aa29576-16/aa29576-16.html`. Published online: 12 December 2016.

[34] D. Souami, J. Cresson, C. Biernacki, and F. Pierret. On the local and global properties of gravitational spheres of influence. *Monthly Notices of the Royal Astronomical Society*, 496(4):4287–4297, 2020.

[35] K. E. Tsiolkovsky. The exploration of outer space by means of rocket devices. *The Science Review vol. 5*, page 128, 1926. Reissue of the works from 1903 and 1911 with some modifications and additions.

[36] D. A. Vallado. *Fundamentals of astrodynamics and applications*, volume 12. Springer Science & Business Media, 2001.

[37] P. R. Weissman. The oort cloud. *Nature*, 344(6269):825–830, 1990.

A | Appendix A

The solutions here are reported from Lubin (2016)[23].

Laser Sail - Non Relativistic solution

Assume a square sail with properties:

- Thickness h
- Size D
- Density ρ
- Bare (no sail) payload mass m_0
- Array size d
- Perfect reflectivity: $\epsilon_r = 1$
- Distance from laser to sail L
- Spot size D_s

Equations relating these properties are as follows:

$$\theta = \frac{2\lambda}{d}$$

$$D_s = L\theta = \frac{2L\lambda}{d}$$

The force or thrust on the sail, represented by F:

$$F = \frac{2P_0}{c} \quad \text{for } D_s < D$$

$$F = \frac{2P_0}{c}\left(\frac{D}{D_s}\right)^2 = \frac{P_0 d^2 D^2}{2cL^2\lambda^2} \quad \text{for } D_s > D$$

1)For $\mathbf{D_s < D}$, where L_0 is the distance where the spot size equals the sail size:

$$L_0 = \frac{dD}{2\lambda}$$

When $D_s < D$, the force F remains constant:

$$F = \frac{2P_0}{c}$$

Using this force to determine velocity:

$$FL_0 = \frac{1}{2}mv^2$$

$$v = \sqrt{\frac{2FL_0}{m}} = \sqrt{2aL_0}$$

Acceleration:

$$a = \frac{F}{m}$$

Where total mass m consists of:

$$m = m_{\text{sail}} + m_0$$

$$m_{\text{sail}} = D^2 h\rho$$

Using this, kinetic energy can be determined as:

$$KE = FL_0 = \frac{P_0 dD}{c\lambda}$$

Velocity at distance L:

$$v(L) = \sqrt{\frac{4P_0 L}{c(D^2 h\rho + m_0)}}$$

When $L = L_0$:

$$v = v_0 = v(L_0) = \sqrt{\left(\frac{2P_0 dD}{c\lambda(D^2 h\rho + m_0)}\right)}$$

Acceleration remains constant when $D_s < D$:

$$a = \frac{F}{m} = \frac{2P_0}{(D^2 h\rho + m_0)c}$$

Time as a function of L:

$$t(L) = \left(\frac{Lc(D^2 h\rho + m_0)}{P_0}\right)^{\frac{1}{2}}$$

When $t = t_0$ time to $v = v_0$):

$$t_0 = \frac{v_0}{a} = \left(\frac{cdD(D^2 h\rho + m_0)}{2P_0\lambda}\right)^{\frac{1}{2}}$$

In the special case where there's no payload mass ($m_0 = 0$):

$$m = m_{\text{sail}} = D^2 h\rho$$

$$v(L) = \sqrt{\frac{4P_0 L}{cD^2 h\rho}}$$

Finally, with no payload mass:

$$v_0 = \left(\frac{4P_0 L}{cD^2 h\rho}\right)^{1/2} = \left(\frac{2P_0 d}{cD^2 h\rho}\right)^{1/2}$$

$$a = \frac{2P_0}{D^2 h\rho c}$$

$$a \propto P_0 D^{-2} h^{-1} \rho^{-1}$$

$$t(L) = v(L)/a = \left(\frac{Lcd^2 h\rho}{P_0}\right)^{1/2}$$

$$t_0 = v_0/a = \left(\frac{LcD^2 h\rho P_0}{P_0}\right)^{1/2} = \left(\frac{cdD^2 h\rho}{2P_0\lambda}\right)^{1/2} = \left(\frac{cdD^3 h\rho}{2P_0\lambda}\right)^{1/2}$$

$$t_0 \propto P_0^{-1/2} D^{3/2} d^{1/2} h^{1/2} \rho^{1/2} \lambda^{-1/2}$$

Note that $v_0 \propto d^{1/2} D^{-1/2} h^{-1/2}$ implies that a smaller reflector is faster.

Why is a smaller reflector faster?

$$v_0 = \left(\frac{2KE}{m}\right)^{1/2} = \left(\frac{2FL_0}{m}\right)^{1/2}$$

$$m \propto D^2, L_0 \propto D$$

If F is constant so $v_0 \propto \frac{1}{\sqrt{D}}$

I want high $v \Rightarrow$ make D small.

Smaller sail is faster IF $\mathrm{m}_0 = 0$. Make sail as
small as possible IF highest speed is the metric and if $m_0 \neq 0$.

(A.1)

With continued illumination, beyond when the laser spot
exceeds the reflector size, the speed increases by
$\sqrt{2}$ larger than v_0. $v_\infty = v(L = \infty) = \sqrt{2}v_0$

(A.2)

$$2) \quad D_s > D, \quad F = \frac{2P}{c}\left(\frac{D}{D_s}\right)^2 = \frac{P_0 d^2 D^2}{2cL^2\lambda^2} = \frac{2P_0}{c}\left(\frac{L_0}{2}\right)^2$$

$$a) D < D_s$$

$$\left(L_0 = \frac{dD_s}{2\lambda}\right)$$

$$KE_{1 \text{ (from } L=0 \text{ to } L_0, D_s = D \text{ or } L = L_0)} = FL_0 =$$

$$= \frac{2P_0L_0}{c} = \frac{P_0 dD}{c\lambda}$$

L_0 is the distance at which $D = D_s$

$$b)KE_{2\text{ from }L=L_0\text{ to }\infty}$$

$$KE_2 = \int_{L_0}^{\infty} F dL = \frac{P_0 d^2 D^2}{2c^2\lambda^2}\int_{L_0}^{\infty}\frac{dL}{L^2} = \frac{P_0 d D'^2}{2c^2}\left(\frac{1}{L_0}-\frac{1}{L}\right)$$

$$= \frac{KE_1 dD}{2\lambda L_0}\left(\frac{1}{L_0}-\frac{1}{L}\right) = KE_1\left(\frac{1}{L_0}-\frac{1}{L}\right) = KE_1 L_0\left(\frac{1}{L_0}-\frac{1}{L}\right) = KE_1\left(1-\frac{L_0}{L}\right),\ \text{as } L \text{ goes to } \infty$$

$$KE_{total} = KE_1 + KE_2 = KE_1\left(2-\frac{L_0}{L}\right) = \frac{2P_0L_0}{c}\left(2-\frac{L_0}{L}\right)$$

$$\rightarrow 2KE_1 = \frac{2P_0dD}{c\lambda} = \frac{4P_0dD}{2c\lambda} = \frac{4P_0L_0}{c} = \frac{2P_02L_0}{c} = F*2L_0 = \frac{1}{2}mv^2 \text{ as } L\rightarrow\infty$$

$$v(L) = \left[\frac{2P_0dD}{mc\lambda}(2-\frac{L_0}{L})\right]^{1/2} = \left[\frac{4P_0L_0}{mc}(2-\frac{L_0}{L})\right]^{1/2}$$

$$v_0 = v(L=L_0) = \left[\frac{2P_0dD}{mc\lambda}\right]^{1/2} = \left[\frac{4P_0L_0}{mc}\right]^{1/2} = [2a_0L_0]^{1/2}$$

$$\text{where } a_0 = \frac{F}{m} = \frac{2P_0}{mc}$$

$$v(L) = \left[\frac{2P_0dD}{mc\lambda}\left(2-\frac{L_0}{L}\right)\right]^{1/2} = v_0\left(2-\frac{L_0}{L}\right)^{1/2} \tag{A.3}$$

$$v_0 = v(L=\infty) = \sqrt{2}v_0 \tag{A.4}$$

$$L_0 = \frac{dD}{2\lambda} \tag{A.5}$$

$$a(L) = \frac{F}{m} = \frac{P_0}{2mc}\left(\frac{dD}{L\lambda}\right)^2 = \frac{2P_0}{mc}\left(\frac{L_0}{L}\right)^2 = a_0\left(\frac{L_0}{L}\right)^2 \tag{A.6}$$

$$v(L) = \left[\frac{2P_0dD}{c(\lambda m_{sail} + m_0)}\right]^{1/2} \left[(2 - \frac{L_0}{L})\right]^{1/2} = \left[\frac{2P_0dD}{c(\lambda D^2h\rho + m_0)}\right]^{1/2} \left[(2 - \frac{L_0}{L})\right]^{1/2} \text{ for } L > L_0 \tag{A.7}$$

Maximizing Speed of Laser driven system

Let $v = v(L)$

For $L = L_0; v(L_0) = v_0 = v_0(D)$

$L_0 = dD/2\lambda$

where D is the sail size and $L = L_0$ when spot size $= D$

$$v_0(D) = \left(\frac{2P_0d}{c\lambda}\frac{D}{D^2h\rho + m_0}\right)^{1/2}$$

$$= \left(\frac{2P_0d}{c\lambda}\frac{D}{m_s + m_0}\right)^{1/2}$$

where $m_s =$ mass sail $= D^2h\rho$

$m_0 =$ payload mass without sail

$v(D)$ limiting cases:

$v_0(D = 0) = 0$

$$\lim_{D\to 0} v_0(D) = 0$$

hence find D to give maximum v_0

set $dv/dD = 0$

$$\frac{dv}{dD} = \frac{1}{2}\left(\frac{D}{D^2h\rho + m_0}\right)^{-1/2}\left(\frac{2Dh\rho + m_0 - D(2Dh\rho)}{(D^2h\rho + m_0)^2}\right) = \frac{1}{2}\left(\frac{D}{m_s + m_0}\right)^{1/2}\left(\frac{m_0 - m_s}{(m_s + m_0)^2}\right)$$

Therefore max v ($dv/dD = 0$) occurs when $m_s = m_0$, (mass sail = payload mass)

Therefore:

$$v_{\max}(m_s = m_0) = \left(\frac{2P_0 d}{c\lambda}\frac{D}{2m_0}\right)^{1/2} = \left(\frac{P_0 d}{c\lambda}\right)^{1/2}\left(\frac{1}{h\rho m_0}\right)^{1/4}$$

(since $D = (m_0/h\rho)^{1/2}$ for $m_{\text{sail}} = m_0$)

$$= \left(\frac{P_0 d}{c\lambda}\right)^{1/2}\left(\frac{1}{(h\rho D)^{1/2}}\right)$$

$$= \left(\frac{P_0}{c\lambda h\rho}\frac{d}{D}\right)^{1/2}$$

$$= c\left(\frac{P_0}{P_1}\frac{d}{D}\right)^{1/2}$$

where $P_1 = c^3\lambda h\rho$ is 2.7×10^{16} watts $\times\ \lambda(\mu\text{m})\ \rho(g/cc)$

Maximizing Speed of Laser driven system

II$(L = \infty)$

$$\lim_{L\to\infty} v(L) = v_0 = v_0\sqrt{2}$$

$$\left.\frac{dv}{dD}\right|_{(L=\infty)} = 0 = \left.\frac{dv}{dD}\right|_{(L=L_0)}\sqrt{2}$$

therefore same condition for max v i.e when $m_s = m_0$

$$\Rightarrow \lim_{L\to\infty} v(L) = v_0 = v_0\sqrt{2} = \left(\frac{2P_0 d}{c\lambda}\right)^{1/2}\left(\frac{1}{h\rho m_0}\right)^{1/4}$$

III (a at $v_{\max}$ when $m_s = m_0$, $m = m_s + m_0 = 2m_s = 2m_0$)

Given that $m = m_s + m_0 = 2m_s = 2m_0$, the acceleration a can be expressed as:

$$a = \frac{F}{m} = \frac{F}{2m_0} = \frac{P_0}{m_0 c} = \frac{P_0}{cD^2 h\rho}$$

And the characteristic time t_0 to reach $v_{\max}$ is:

$$t_0 = \frac{v_{\max}}{a} = \left(\frac{cdD^2h\rho}{P_0\lambda}\right)^{1/2} = \left(\frac{cdD^2h\rho}{P_0\lambda}\right)^{1/2} \tag{A.8}$$

Resulting in:

$$t_0 = \left(\frac{cdDm_0}{P_0\lambda}\right)^{1/2} = \left(\frac{cd}{\lambda}\left(\frac{m_0^3}{h\rho}\right)^{1/4}\right) \tag{A.9}$$

Where:

$$D = (m_0/h\rho)^{1/2}$$

$$L_0 = dD/2\lambda$$

t_0 is the time when the spot size = sail size.

Relativistic solution

The solution here reported is otbained in Kulkarni (2018) [21]. Conservation of 4-momentum in the context of a directed energy system for spacecraft propulsion is described by the following equation, assuming the spacecraft system remains in an inertial frame:

$$\tilde{p}_0^\mu + p_0^\mu = \tilde{p}_f^\mu + p_f^\mu \tag{A.10}$$

The components of the 4-momentum conservation are given explicitly as:

$$\begin{bmatrix} E_0 + \sqrt{m^2 + p_0^2} \\ E_0 + p_0 \end{bmatrix} = \begin{bmatrix} E_f + \sqrt{m^2 + p_f^2} \\ E_f + p_f \end{bmatrix} \tag{A.11}$$

The equations for the spacecraft's initial and final total energy and momentum are:

$$\begin{aligned} p_0(E_0) =& (4E_0^2 + 4E_0p_0 - m^2)^{-1}\Bigg(4E_0^3 + 2E_0\left(\sqrt{E_0^2(m^2+p_0^2)} - m^2 + p_0^2\right) \\ &+ p_0\left(2\sqrt{E_0^2(m^2+p_0^2)} - m^2\right) + 6E_0p_0\Bigg). \end{aligned} \tag{A.12}$$

The change in 4-momentum of the spacecraft in time dt is given by:

$$\frac{dp^\mu}{dt} = \Gamma \Delta p^\mu \left(1 - \frac{p}{\sqrt{m^2 + p^2}}\right). \tag{A.13}$$

The number of photons striking the sail in the DE system's frame over time dt is:

$$dN = (1 - v)\Gamma dt \left(1 - \frac{p}{\sqrt{m^2 + p^2}}\right) \Gamma dt. \tag{A.14}$$

The energy of the photons in terms of dimensionless photon energy ϵ is:

$$|E_f| = \left(\frac{1 - \beta}{1 + \beta}\right) |E_i|. \tag{A.15}$$

As we are interested in the soft photon limit where the photon energy is much less than the rest mass energy of the spacecraft ($\epsilon \ll 1$), we primarily work to first order in ϵ:

$$\Delta p' = p_f - p_i = p_c \epsilon \tag{A.16}$$

The rate of change of the spatial component of the spacecraft's momentum is given by:

$$\frac{dp'_1}{dt} = \frac{d}{dt}(m\gamma v) = 2P \left(\frac{1 - v}{1 + v}\right) \tag{A.17}$$

Restoring factors of c and defining $\beta = v/c$, the equation can be rewritten as:

$$\dot{\beta} = \frac{2P}{mc^2\gamma^3} \left(\frac{1 - \beta}{1 + \beta}\right) \tag{A.18}$$

Including the diffraction effects, equation A.18 becomes:

$$\dot{\beta} = \begin{cases} \frac{2P}{mc^2\gamma^3} \left(\frac{1-\beta}{1+\beta}\right), & x \leq L_0 \\ \frac{2P}{mc^2\gamma^3} \left(\frac{1-\beta}{1+\beta}\right) \left(\frac{L_0}{x}\right)^2, & x > L_0 \end{cases} \tag{A.19}$$

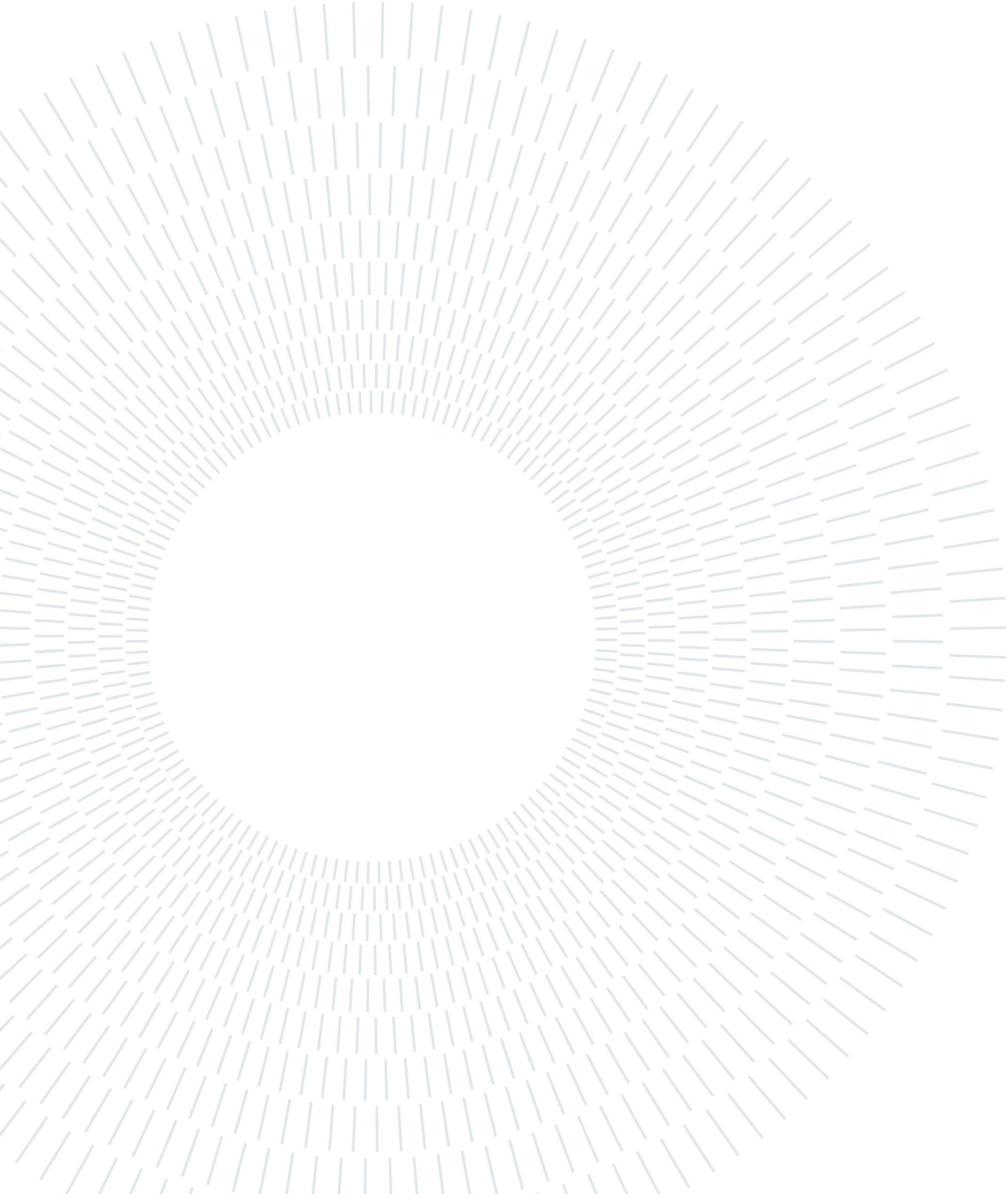

B | Appendix B

This is a summary of the Galactic potential model described in Irrgang [18]:

Galactic Potential Model

The following equations are obtained from Piotr A. Dybczy´nski [10] using the Galactic potential model (Model I) from Irrgang et al. [18].

The Galactic gravitational potential is essential for understanding the dynamics and structure of the Milky Way. It is conventionally decomposed into three components: the central bulge Φ_b, the axisymmetric disk Φ_d, and the dark matter halo Φ_h. Each component is defined by a specific potential function that contributes to the overall gravitational field experienced by objects within the Galaxy.

Central Bulge Potential

The potential $\Phi_b(R)$ of the central bulge is modeled as a spherically symmetric component, which is mathematically expressed as:

$$\Phi_b(R) = -\frac{M_b}{\sqrt{R^2 + b_b^2}} \tag{B.1}$$

where R is the Galactocentric spherical radius, M_b is the total mass of the bulge, and b_b is a characteristic scale length that defines the bulge's density profile.

Axisymmetric Disk Potential

The disk potential $\Phi_d(r, z)$ is axisymmetric and described by:

$$\Phi_d(r, z) = -\frac{M_d}{\sqrt{r^2 + \left(a_d + \sqrt{z^2 + b_d^2}\right)^2}} \tag{B.2}$$

In this expression, r and z are the Galactocentric cylindrical coordinates, respectively the distance from the centre of the Galaxy and the z component, M_d represents the mass of the disk, a_d is the disk's radial scale length, and b_d is the scale height of the disk.

Dark Matter Halo Potential

The dark matter halo potential $\Phi_h(R)$, which includes the contribution from dark matter distributed throughout the Galaxy, is given by a more complex formula that reflects the mass distribution inferred from observations of the Galactic rotation curve. For regions where the Galactocentric radius R is less than a cutoff $\Lambda = 200$ kpc, the halo potential is modeled as:

$$\Phi_h(x, y, z) = -\frac{M_h}{a_h}\left(\ln\left(\frac{a_h + \sqrt{x^2 + y^2 + z^2}}{a_h + \Lambda}\right) - \frac{\Lambda}{a_h + \Lambda}\right). \tag{B.3}$$

for $R < \Lambda$, and it takes a constant value beyond this cutoff. Here, M_h denotes a scaling factor related to the halo mass, a_h is a scale length, and Λ is introduced to prevent the divergence of the halo mass at large radii. The choice of these parameters is motivated by the flat rotation curves observed in the outer parts of the Galaxy, suggesting a mass distribution that grows linearly with radius at large scales.

The complete gravitational potential of the Milky Way is therefore represented as the sum of these three components, each crucial for simulating and predicting the motion of stars and other objects within the Galaxy.

Equations of Motion

The motion of a star within this gravitational potential is governed by the equations of motion derived from the potential gradients. These equations, in a rectangular Galactic coordinate system, are given by:

$$\ddot{x} = -\frac{\partial \Phi_b}{\partial x} - \frac{\partial \Phi_d}{\partial x} - \frac{\partial \Phi_h}{\partial x} \tag{B.4}$$

$$\ddot{y} = -\frac{\partial \Phi_b}{\partial y} - \frac{\partial \Phi_d}{\partial y} - \frac{\partial \Phi_h}{\partial y} \tag{B.5}$$

$$\ddot{z} = -\frac{\partial \Phi_b}{\partial z} - \frac{\partial \Phi_d}{\partial z} - \frac{\partial \Phi_h}{\partial z} \tag{B.6}$$

where x, y, and z represent the coordinates of the star in the Galactic frame, and $\ddot{x}$, $\ddot{y}$, $\ddot{z}$ are the respective accelerations.

$$\frac{\partial \Phi_b(x,y,z)}{\partial x} = -\frac{xM_b}{(x^2+y^2+z^2+b_b^2)^{3/2}}, \tag{B.7}$$

$$\frac{\partial \Phi_b(x,y,z)}{\partial y} = -\frac{yM_b}{(x^2+y^2+z^2+b_b^2)^{3/2}}, \tag{B.8}$$

$$\frac{\partial \Phi_b(x,y,z)}{\partial z} = -\frac{zM_b}{(x^2+y^2+z^2+b_b^2)^{3/2}}. \tag{B.9}$$

$$\frac{\partial \Phi_d(x,y,z)}{\partial x} = -\frac{xM_d}{\left(x^2+y^2+(a_d+\sqrt{z^2+b_d^2})^2\right)^{3/2}}, \tag{B.10}$$

$$\frac{\partial \Phi_d(x,y,z)}{\partial y} = -\frac{yM_d}{\left(x^2+y^2+(a_d+\sqrt{z^2+b_d^2})^2\right)^{3/2}}, \tag{B.11}$$

$$\frac{\partial \Phi_d(x,y,z)}{\partial z} = -\frac{zM_d\left(a_d+\sqrt{z^2+b_d^2}\right)}{\left(\sqrt{z^2+b_d^2}\right)\left(x^2+y^2+(a_d+\sqrt{z^2+b_d^2})^2\right)^{3/2}}. \tag{B.12}$$

$$\frac{\partial \Phi_h(x,y,z)}{\partial x} = -\frac{xM_h}{a_h\sqrt{x^2+y^2+z^2}\left(a_h+\sqrt{x^2+y^2+z^2}\right)}, \tag{B.13}$$

$$\frac{\partial \Phi_h(x,y,z)}{\partial y} = -\frac{yM_h}{a_h\sqrt{x^2+y^2+z^2}\left(a_h+\sqrt{x^2+y^2+z^2}\right)}, \tag{B.14}$$

$$\frac{\partial \Phi_h(x,y,z)}{\partial z} = -\frac{zM_h}{a_h\sqrt{x^2+y^2+z^2}\left(a_h+\sqrt{x^2+y^2+z^2}\right)}. \tag{B.15}$$

where $\sqrt{x^2+y^2+z^2} = R$ is the Galactocentric spherical radius.

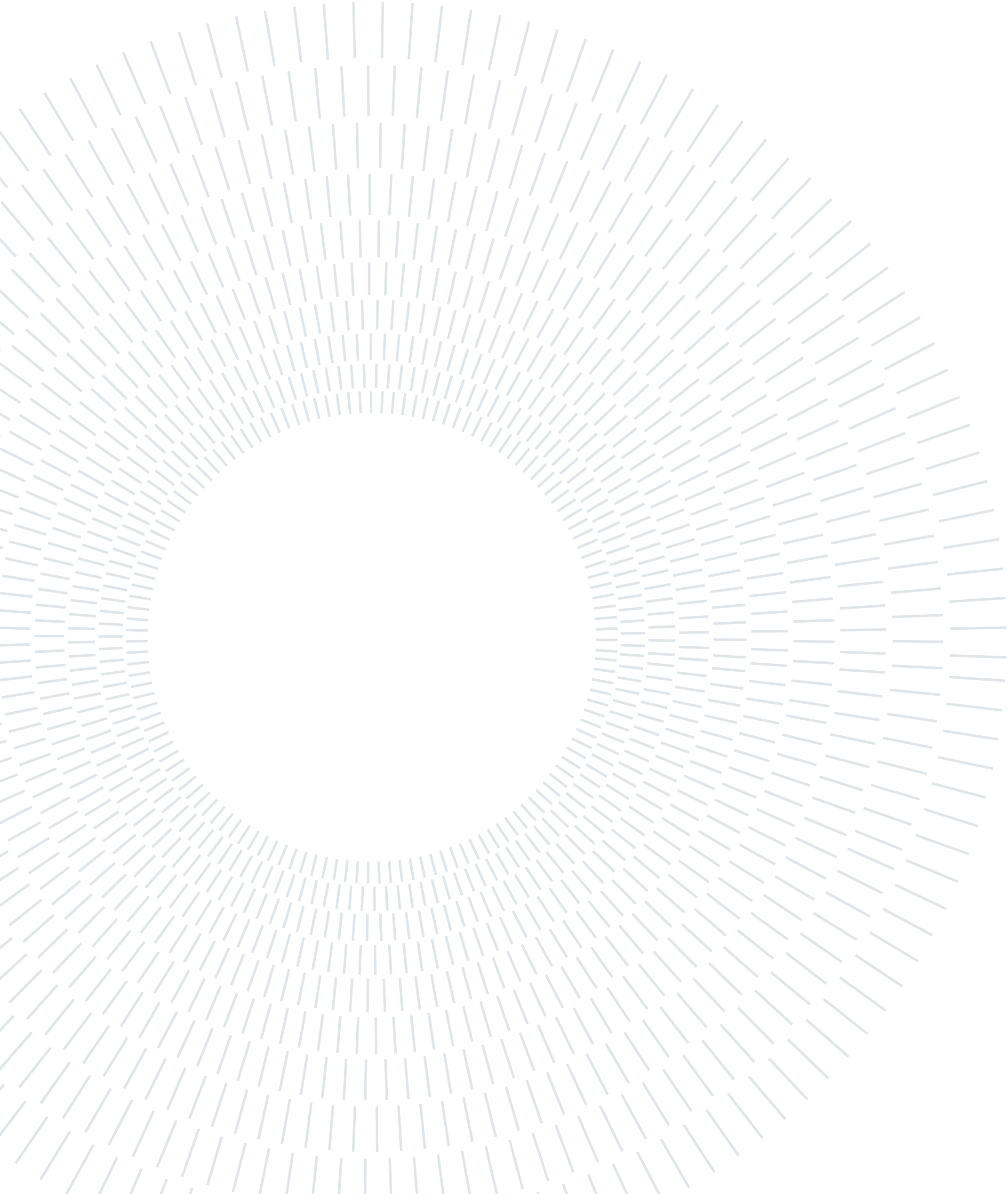

List of Figures

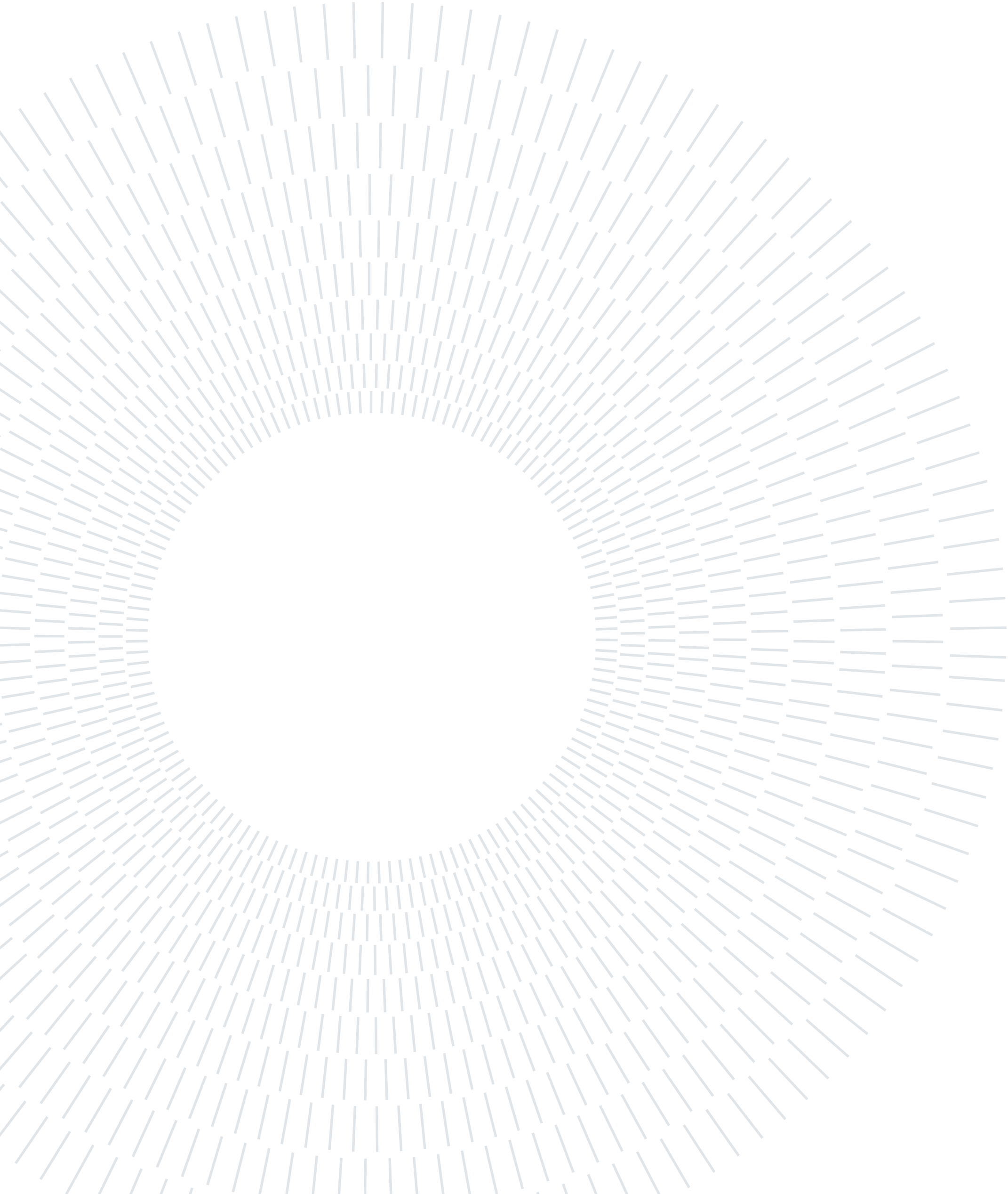

List of Tables

List of Symbols

Symbol	**Description**	**Unit**
D_s	Laser spot size	m
ϵ_r	Reflection coefficient	-
P	Laser power	W
c	Speed of light	m/s
θ	Beam divergence	rad
λ	Wavelength of the laser	m
d	DE array size or diameter of the laser system	m
L	Distance from laser to sail	m
L_0	Distance where laser spot equals spacecraft size	m
D	Side length of a square sail or size of the sail	m
m_{sail}	Mass of the sail	kg
m_{payload}	Mass of the payload	kg
m_0	Rest mass of the spacecraft	kg
h	Thickness of the sail	m
ρ	Density of the sail material	kg/m^3
F	Force applied by an incident laser on a surface	N
Mb, Md, Mh	Galactic bulge, disk, halo mass parameters	$M_\odot$
b_b, a_d, b_d, a_h	Galactic model characteristic distances	pc
γ	Lorentz factor	-
β	Ratio of spacecraft speed to the speed of light	-
v	Velocity of the spacecraft	m/s
KE	Kinetic energy	J

Symbol	Description	Unit
t	Time	s
R	Galactocentric spherical radius	pc
σ	Standard deviation	deg,s
μ	Gravitational parameter	$\mathrm{m}^3/\mathrm{s}^2$
r	Cylindrical coordinate in the plane of the Galaxy	pc
$\alpha_{\text{optimal}}, \delta_{\text{optimal}}$	Optimal right ascension, declination coordinates	deg
$\mathbf{d}$	Position vector of spacecraft relative to Earth	km
$\boldsymbol{\rho}$	Position vector of Earth relative to the Sun	km
$\mathbf{r}$	Position vector of spacecraft relative to the Sun	km
d_P	Distance of Proxima Centauri from the Sun	pc
$\mathbf{r}_{P,h}$	Heliocentric equatorial position vector of Proxima Centauri	pc
α	Right ascension of Proxima Centauri	degrees
δ	Declination of Proxima Centauri	degrees
π	Parallax of Proxima Centauri	mas
$\mu_{*\alpha}$	Proper motion in right ascension of Proxima Centauri	mas/year
μ_δ	Proper motion in declination of Proxima Centauri	mas/year
v_r	Radial velocity of Proxima Centauri	km/s
$\mathbf{r}_{P,h,galactic}$	Heliocentric galactic position vector of Proxima Centauri	pc
$\mathbf{R_x}, \mathbf{R_{z1}}, \mathbf{R_{z2}}$	Rotation matrices for coordinate transformation	-
$\theta_x, \theta_{z1}, \theta_{z2}$	Angles for coordinate transformation in galactic frame	degrees
$\mathbf{A_G}$	Total rotation matrix for galactic coordinates	-
$\mathbf{R_P}$	Galactocentric position vector of Proxima Centauri	pc
R_{Hill}	Hill sphere radius of the Solar System	pc
G	Gravitational constant	$\mathrm{m}^3\mathrm{kg}^{-1}\mathrm{s}^{-2}$
$m_\odot$	Mass of the Sun	kg
$m_\oplus$	Mass of the Earth	kg
c_1, c_2	Constants in the relativistic N-Body problem	-

Symbol	Description	Unit
$\mathbf{M}_{ij}^{\textcircled{1}}, \mathbf{M}_{ij}^{\textcircled{2}}$	Matrices in the relativistic N-Body problem	-
$\mathbf{a}_{\text{Rel},i}$	Relativistic acceleration term	km/s^2
$\mathbf{r}_i, \mathbf{r}_j$	Position vectors in the relativistic N-Body problem	km
$\dot{\mathbf{r}}_i, \dot{\mathbf{r}}_j$	Velocity vectors in the relativistic N-Body problem	km/s
R_{SOI}	Sphere of Influence radius	km
P_0	Initial power of the laser system	W
E_0	Initial kinetic energy in non-relativistic solution	J
a	Acceleration of the spacecraft	m/s^2
t_0	Critical time condition in non-relativistic solution	s
$v(L)$	Velocity of the spacecraft at distance L	m/s
v_0	Velocity of the spacecraft at distance L_0	m/s
$x_{P_{ICRS}}, y_{P_{ICRS}}, z_{P_{ICRS}}$	ICRS coordinates of Proxima Centauri	pc
d_P	Distance of Proxima Centauri in parsec	pc
σ_{pointing}	Standard deviation in pointing errors	arcsec
$t_{\text{propulsion}}$	Propulsion time duration	s
v_∞	Maximum achievable velocity of the sail	m/s
$\hat{\mathbf{dir}}_{\text{target}}$	Unit vector in the direction of the target	-
$\mathbf{s}_0$	Initial state vector of the spacecraft	km, km/s
$\mathbf{r}_0$	Initial position vector of the spacecraft	km
$\mathbf{v}_0$	Initial velocity vector of the spacecraft	km/s
$\mathbf{a}_{\text{sc}}$	Total acceleration of the spacecraft	km/s^2
$\mathbf{a}_{\text{gravity}}$	Gravitational acceleration acting on the spacecraft	km/s^2
$\mathbf{a}_{\text{laser}}$	Acceleration due to laser propulsion	km/s^2
$\mathbf{r}_{\oplus\text{sc}}$	Position vector of spacecraft relative to Earth	km
$\mathbf{r}_{\odot\oplus}$	Position vector of Earth relative to the Sun	km
$\mathbf{r}$	Heliocentric position vector of the spacecraft	km
R	Galactocentric spherical radius	pc
r	Cylindrical coordinate in the plane of the Galaxy	pc
ϵ	Angle error during trajectory propagation	degrees

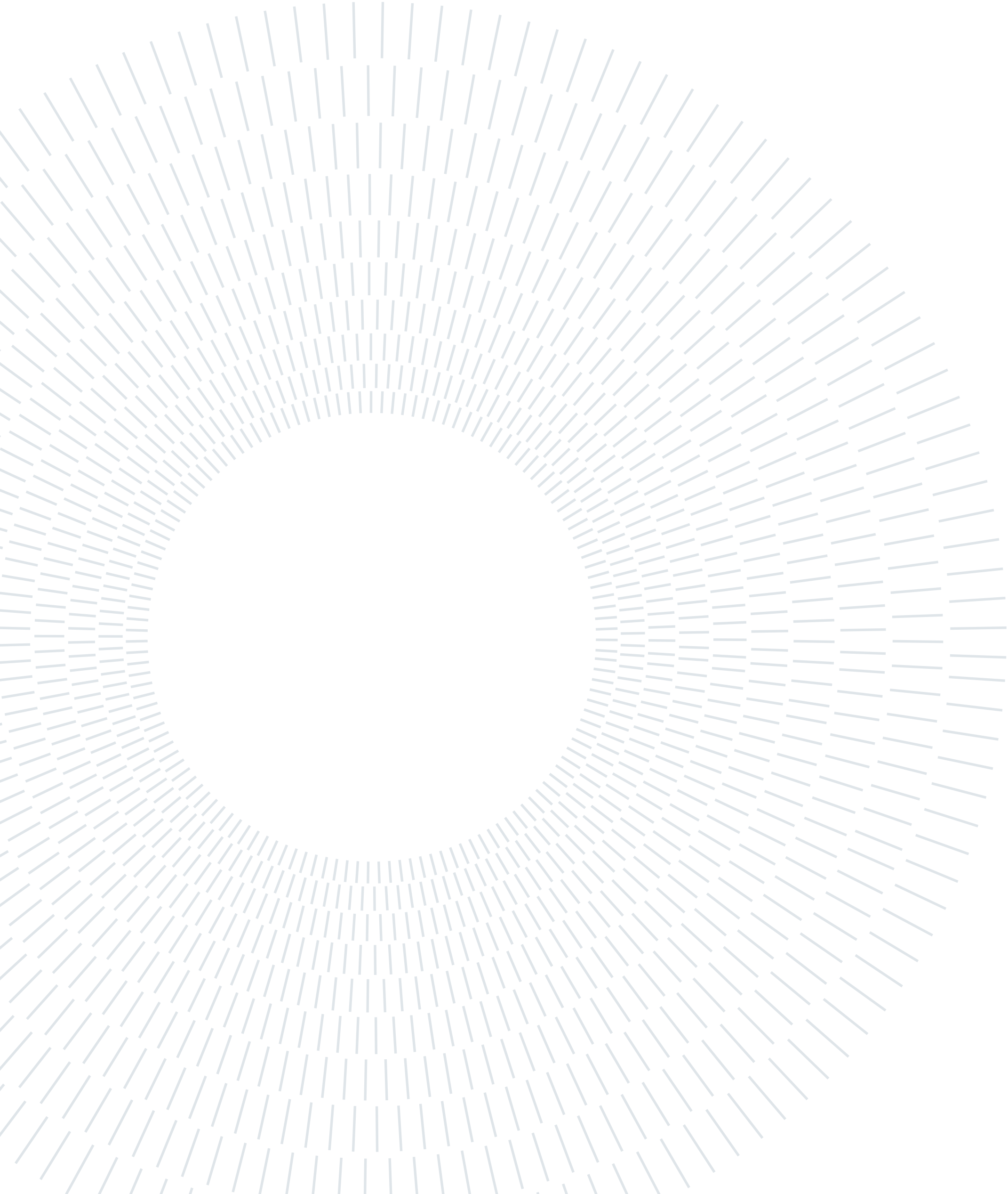

Acknowledgements

Ringrazio i miei genitori per non avermi mai fatto mancare nulla durante i miei anni all'università e per l'amore che mi ha sempre motivato e dato la forza per superare gli ostacoli; in particolare grazie mamma, per avermi fatto scoprire la meraviglia dell'esplorazione dell'Universo.

Grazie ai miei fratelli, siete i migliori amici che ho. Ma anche grazie ai miei amici, che talvolta sono come dei fratelli.

Sono estremamente fortunato ad avere dei nonni che hanno sempre fatto il tifo per me per tutto il percorso, sempre i primi a voler sapere l'esito degli esami, o semplicemente a chiedermi come stessi o come mi sentissi. Sono domande semplici ma profonde e che tendiamo tutti a trascurare nella quotidianità. Grazie.

Grazie zii per essere i migliori amici in famiglia, è una fortuna poter contare sempre su di voi e sulla vostra vicinanza.

Infine vorrei ringraziare Gloria, compagna di vita con la quale ho condiviso il percorso universitario presente ma anche quello scolastico. Con te ho imparato ad essere una persona più buona, più calma e in generale mi hai sempre reso una persona migliore. Spero solo di aver ricambiato tutto l'amore e il bene che mi hai dato. Sono sicuro che sorreggerci e sostenerci sia dentro che fuori lo studio ci abbia reso così forti e consapevoli, e che da qualsiasi momento abbiamo sempre tratto il meglio di noi.